# Sparse Equation Matching: A Derivative-Free Learning for General-Order Dynamical Systems

Jiaqiang Li
School of Management
University of Science and Technology of China
Anhui, Hefei, China,
Jianbin Tan
Department of Biostatistics & Bioinformatics
Duke University, Durham, NC, USA,
and
Xueqin Wang\*
School of Management
University of Science and Technology of China
Anhui, Hefei, China

#### Abstract

Equation discovery is a fundamental learning task for uncovering the underlying dynamics of complex systems, with wide-ranging applications in areas such as brain connectivity analysis, climate modeling, gene regulation, and physical system simulation. However, many existing approaches rely on accurate derivative estimation and are limited to first-order dynamical systems, restricting their applicability to realworld scenarios. In this work, we propose sparse equation matching (SEM), a unified framework that encompasses several existing equation discovery methods under a common formulation. SEM introduces an integral-based sparse regression method using Green's functions, enabling derivative-free estimation of differential operators and their associated driving functions in general-order dynamical systems. The effectiveness of SEM is demonstrated through extensive simulations, benchmarking its performance against derivative-based approaches. We then apply SEM to electroencephalographic (EEG) data recorded during multiple oculomotor tasks, collected from 52 participants in a brain-computer interface experiment. Our method identifies active brain regions across participants and reveals task-specific connectivity patterns. These findings offer valuable insights into brain connectivity and the underlying neural mechanisms.

Keywords: Brain connectivity, Equation discovery, Electroencephalographic data, General-order dynamic, Green's function

<sup>\*</sup>Email of correspondence: wangxq20@ustc.edu.cn

### 1 Introduction

Modeling dynamics of complex systems is central to many fields, including neuroscience (Kiebel et al., 2009; Zhang et al., 2020), physics (Ramsay and Hooker, 2017; Brunton et al., 2016), epidemiology (Tan et al., 2022; Tian et al., 2021), climate science (Lorenz, 2017; Brunton et al., 2016), and gene regulation (Wu et al., 2014; Dai and Li, 2022). In many of these domains, the system dynamics are naturally formulated as ordinary differential equations (ODEs), which establish a model for the time derivatives of dynamic data to characterize system evolutions and underlying mechanisms. ODEs provide a principled and flexible framework to represent continuous-time dynamics that govern many real-world phenomena. However, despite their widespread utility, the exact forms of these equations are usually unknown or only partially understood (Wu et al., 2014; Brunton et al., 2016). This motivates the task of equation discovery, aiming to learn the governing equations of complex systems from dynamic data.

Formally, we focus on the equation discovery of an ODE with the form:

$$\mathcal{P}_i X_i(t) = f_i(\boldsymbol{X}(t), t), \quad i = 1, \dots, p,$$
(1)

where  $\mathbf{X}(t) := (X_1(t), \dots, X_p(t))^{\top}$  represents the data of p-dimensional state variables observed over time,  $\mathcal{P}_i$  denotes a differential operator that defines the structure of the derivative to be modeled, and  $f_i$  is an unknown driving function to be learned from the data. This formulation differs from traditional parameter estimation in dynamical systems, where  $f_i$  are assumed to follow a fixed parametric form, usually informed by prior domain knowledge (Ramsay et al., 2007; Dattner and Klaassen, 2015; Ramsay and Hooker, 2017; Yang et al., 2021; Tan et al., 2023; Shao and Yao, 2025). By relaxing this assumption, equation discovery offers a more flexible, data-driven approach that can adapt to observed patterns and

potentially uncover new mechanistic insights.

In the following, we present several real-world examples to illustrate the task of equation discovery.

Example 1 (Brain Connectivity Discovery). Human brain activity is often recorded using electroencephalography (EEG) data (Niedermeyer and da Silva, 2005), providing time-resolved signals that capture complex patterns of connectivity across distinct brain regions (Friston, 2011). Such connectivity is naturally described by ODEs, which determine how the state of each region evolves and interacts with others. In this context, discovering brain connectivity becomes a problem of identifying the governing equations from time-resolved data—a typical equation discovery task. This perspective provides a useful method for the effective identification of brain connectivity (Kiebel et al., 2009; Valdes-Sosa et al., 2011; Zhang et al., 2017, 2020).

Example 2 (Climate Dynamics Discovery). Climate systems are often studied using time-series data such as temperature, atmospheric pressure, and wind speed, which reflect complex, nonlinear interactions across spatial and temporal scales (Stein et al., 2014; Lorenz, 2017). These interaction mechanisms are commonly characterized by ODEs, which model how climate variables co-evolve over time and space. Recently, equation discovery methods have been successfully applied to uncover such ODEs in climate systems, including the recovery of canonical structures like Lorenz systems (Brunton et al., 2016) and the Van der Pol oscillator (Owens and Kutz, 2023).

Example 3 (Interaction Law Discovery). Inferring interaction laws from agent-based dynamic data is a fundamental problem across many scientific disciplines (Lu et al., 2019). These systems, composed of multiple interacting agents, often exhibit interactions that strongly depend on pairwise distances between agents, such as particle interactions in physics (Carrillo et al., 2017). Discovering these laws aligns closely with the broader goal of equation

discovery, enabling mechanistic understanding of complex systems. Such approaches enhance the ability to predict and simulate dynamic phenomena across diverse domains, including biology, physics, and social systems (Lu et al., 2021; Brückner and Broedersz, 2024).

Other examples of equation discovery can be found in gene regulation, social sciences, and economics (Chen et al., 2017; Brunton and Kutz, 2022; Dai and Li, 2022; Balla et al., 2025).

To solve the above equation discovery tasks, one widely adopted method is to regress the derivatives of system trajectories onto the trajectories themselves (Wu et al., 2014; Brunton et al., 2016; Zhang et al., 2017; Lu et al., 2019). These approaches view the equation discovery for ODE (1) as a continuous-time analogue of autoregressive modeling in time series analysis (Shumway et al., 2000), where the discrete temporal differences in the time series framework are extended to infinitesimal derivatives in ODEs. From this perspective, accurate estimation of derivatives becomes crucial, as they serve as the response variables in the regression framework.

Despite the effectiveness of the regression-based framework, most existing literature focuses on equation discovery for first-order systems, i.e., learning driving functions for the first-order derivatives of the data. Although such methods can, in principle, be extended to higher-order systems, they require the estimation of higher-order derivatives for learning the associated driving functions. This requirement poses significant challenges for equation discovery, as higher-order derivative estimation is usually unstable and sensitive to noise (Wahba, 1990).

To mitigate the reliance on derivative estimation, integration-based regression approaches have been applied in various equation discovery settings (Chen et al., 2017; Messenger and Bortz, 2021; Qian et al., 2022; Dai and Li, 2022). These methods utilize integral formulations to reformulate differential equations, thereby eliminating the dependence on first-order

derivatives in the learning task. However, for general-order dynamical systems, simple integration is often insufficient to fully eliminate the need for derivative estimation. This insufficiency hinders the applicability of equation discovery in settings involving complex high-order dynamics, which commonly arise in applications such as brain connectivity identification, climate dynamics modeling, and interaction law inference (Zhang et al., 2020; Owens and Kutz, 2023; Lu et al., 2021) in Examples 1 – 3.

To solve the above challenges, we propose a novel equation discovery method tailored for general-order dynamical systems, generalizing the Green's matching approach (Tan, Zhang, Wang, Huang and Yao, 2024) for parameter estimation to differential equation learning. Our method employs extended integral formulas for general-order ODEs using Green's functions (Duffy, 2015), providing a foundation for converting ODEs into integral equations of arbitrary order. This transformation unifies existing derivative-based and integral-based approaches (Brunton et al., 2016; Chen et al., 2017; Brunton and Kutz, 2022; Dai and Li, 2022) within a single framework, introducing a broader class of equation discovery methods that were previously unavailable. The unified framework offers a direct way to eliminate derivatives from the governing equations, leading to a new equation discovery method that is free of derivative estimation.

Secondly, we extend the concept of sparsity in regression models (Hastie et al., 2017) to our framework, in line with existing work on equation discovery (Brunton et al., 2016; Brunton and Kutz, 2022). We refer to our method as sparse equation matching (SEM), an integral-based sparse regression approach for statistical learning of differential equations. A key distinction of SEM from existing methods is its ability to estimate both the differential operator  $\mathcal{P}_i$  of a linear form and the driving function  $f_i$  in (1) simultaneously, without explicit estimation of data derivatives. This leads to a more accurate framework for equation discovery in general-order dynamical systems, as evidenced by our simulation studies.

Third, we apply SEM to electroencephalographic (EEG) data, collected during oculomo-

tor tasks from 52 participants in a brain-computer interface experiment (Cho et al., 2017). We first demonstrate the effectiveness of SEM in predicting EEG signals across three oculomotor tasks: eye blinking, horizontal eye movement, and vertical eye movement. Subsequently, we use SEM to infer population-level brain networks from the EEG data, uncovering both distinct and overlapping connectivity patterns associated with each task. These findings provide insights into the intrinsic neural mechanisms underlying oculomotor behavior, highlighting the potential of SEM to advance research in brain connectivity analysis.

The remainder of this article is organized as follows. In Section 2, we introduce an equation matching framework for general-order dynamical systems, aiming to unify several existing equation discovery methods under a common formulation. Based on this, Section 3 presents the proposed SEM method, detailing its implementation algorithm and key estimation properties. To evaluate the performance of SEM, Section 4 provides simulation studies comparing SEM with derivative-based approaches. We then apply SEM to EEG data collected during oculomotor tasks in Section 5, demonstrating its utility for both signal prediction and brain connectivity discovery. Finally, we conclude the paper and outline potential directions for future research in Section 6.

### 2 Methodology

Notation Denote  $\frac{\mathrm{d}^k}{\mathrm{d}t^k}$  as the differential operator that extracts the k-th derivative of a function. Let  $L^2(\mathcal{T})$  be the space of square-integrable functions on a domain  $\mathcal{T}$ , equipped with the standard  $L^2$  norm  $\|\cdot\|_{L^2}$  and inner product  $\langle\cdot,\cdot\rangle$ . Define the null space of an operator  $\mathcal{P}$  as  $\mathrm{Ker}(\mathcal{P}) := \{g(\cdot) \mid \mathcal{P}g(\cdot) \text{ is a zero function}\}$ . Let  $\mathbb{I}(\cdot)$  be the indicator function and  $\delta(\cdot)$  be the Dirac delta function concentrated at zero. Define  $(\cdot)_+$  as  $\max\{\cdot,0\}$ . We use the notation  $\|\cdot\|$  to denote the Euclidean norm. In what follows, we may simplify a function  $f(\cdot)$  as f.

We introduce some preliminary concepts relevant to reproducing kernel Hilbert spaces (RKHS). Let  $\mathcal{H}$  be a Hilbert space of functions defined on a domain  $\mathcal{T}$ , equipped with inner product  $\langle \cdot, \cdot \rangle_{\mathcal{H}}$  and the corresponding norm  $\|\cdot\|_{\mathcal{H}}$ . The space  $\mathcal{H}$  is called a RKHS if there exists a kernel function  $\mathcal{K}: \mathcal{T} \times \mathcal{T} \to \mathbb{R}$  such that  $\mathcal{K}(t, \cdot) \in \mathcal{H}$  for all  $t \in \mathcal{T}$ , and the reproducing property holds:

$$f(t) = \langle f, \mathcal{K}(t, \cdot) \rangle_{\mathcal{H}}, \quad \forall f \in \mathcal{H}, \ t \in \mathcal{T}.$$

Since K is uniquely associated with the space  $\mathcal{H}$ , we refer to K as the reproducing kernel of the Hilbert space, and denote  $\mathcal{H}$  by  $\mathcal{H}(K)$ .

**Basic Setting** Assume we collect the observed data  $\{Y_{ij}\}_{i=1,\dots,p,\ j=1,\dots,n}$ , which follows:

$$Y_{ij} = X_i(t_j) + \epsilon_{ij} \tag{2}$$

for  $i=1,\ldots,p,\ j=1,\ldots,n,\ t_j\in[0,C]$ , where  $\epsilon_{ij}$ s are mean-zero white noise,  $X_i(t)$  denotes the value of the trajectory  $X_i$  at time  $t,\ \{t_j\}_{j=1}^n\subset[0,C]$  is the observed time points for  $X_i$ , n is the number of observed time points, and p is the number of trajectories. Let  $X_i(t),\ i=1,\ldots,p$ , be smooth functions over  $t\in[0,C]$ , which satisfy the differential equations:

$$\mathcal{P}_i^K X_i(t) = f_i(\boldsymbol{X}(t), t), \quad i = 1, \dots, p,$$
(3)

where  $\boldsymbol{X}(t) := (X_1(t), \dots, X_p(t))^{\top}$  denotes the vector of state variables at time t, and  $f_i$ ,  $i = 1, \dots, p$ , represent driving functions that produce the dynamics of  $\boldsymbol{X}$ . The differential operator  $\mathcal{P}_i^K$  is of the form:

$$\mathcal{P}_i^K = \frac{\mathrm{d}^K}{\mathrm{d}t^K} + \sum_{l=1}^{K-1} \omega_{il} \frac{\mathrm{d}^l}{\mathrm{d}t^l},\tag{4}$$

which is a linear differential operator of order K. Such forms of differential operators have been adopted in many real-world applications (Meirovitch, 2010; Ramsay and Hooker, 2017; Zhang et al., 2020; Shao and Yao, 2025). We assume that K is fixed and known.

Let  $\mathbf{f} := (f_1, \dots, f_p)^{\top}$ ,  $\boldsymbol{\omega}_i := (\omega_{i1}, \dots, \omega_{i(K-1)})^{\top}$  and  $\boldsymbol{\omega} := (\boldsymbol{\omega}_i^{\top}, \dots, \boldsymbol{\omega}_p^{\top})^{\top}$ . Our goal is to identify the driving functions  $\mathbf{f}$  and the coefficients  $\boldsymbol{\omega}$  given the observed dynamic data  $Y_{ij}$ s—a standard equation discovery task.

#### 2.1 Equation Matching for General-Order Systems

In this subsection, we propose a new estimation framework for the equation discovery task. Denote  $\frac{\mathrm{d}^{l} \boldsymbol{X}}{\mathrm{d}t^{l}} := \left(\frac{\mathrm{d}^{l} X_{1}}{\mathrm{d}t^{l}}, \dots, \frac{\mathrm{d}^{l} X_{p}}{\mathrm{d}t^{l}}\right)^{\top}$  as the vector of the l-th derivatives of the dynamic trajectories. First, we construct an operator  $\mathcal{F}_{f,\omega}$  that maps the function  $\boldsymbol{X}$  and its derivatives  $\frac{\mathrm{d}\boldsymbol{X}}{\mathrm{d}t}, \dots, \frac{\mathrm{d}^{K}\boldsymbol{X}}{\mathrm{d}t^{K}}$  to the zero vector:

$$\mathcal{F}_{f,\omega}\left(\boldsymbol{X}, \frac{\mathrm{d}\boldsymbol{X}}{\mathrm{d}t}, \dots, \frac{\mathrm{d}^{K}\boldsymbol{X}}{\mathrm{d}t^{K}}, t\right) = \boldsymbol{0}, \quad \forall t \in [0, C].$$
 (5)

Since the operator  $\mathcal{F}_{f,\omega}$  explicitly depends on f and  $\omega$ , it imposes constraints on the trajectory X and its derivatives. Following this, we construct a loss function by integrating these equation constraints from different times:

$$\int_{0}^{C} \left\| \mathcal{F}_{f,\omega} \left( \boldsymbol{X}, \frac{\mathrm{d} \boldsymbol{X}}{\mathrm{d} t}, \dots, \frac{\mathrm{d}^{K} \boldsymbol{X}}{\mathrm{d} t^{K}}, t \right) \right\|^{2} \nu(t) \, \mathrm{d} t, \tag{6}$$

where  $\nu(\cdot)$  is a positive weighting function that assigns a weight to each time point t. If  $X, \frac{dX}{dt}, \dots, \frac{d^KX}{dt^K}$  are available, we can then estimate f and  $\omega$  by minimizing them from the loss in (6).

The above procedure is referred to as equation matching for ODE models, which was first proposed for parameter estimation in differential equations (Tan, Zhang, Wang, Huang and Yao, 2024) and we here extend it to a more general equation discovery setting. One key benefit of this framework lies in its computational efficiency. Specifically, the approach involves matching the trajectories X,  $\frac{dX}{dt}$ , ...,  $\frac{d^KX}{dt^K}$ —which are usually estimated from observed data  $Y_{ij}$ —to the constraint in (5). This facilitates statistical inference without the need to solve the ODE system explicitly, thereby reducing the computational burden associated with ODE model estimation (Tan, Zhang, Wang, Huang and Yao, 2024).

In the following, we introduce the estimation steps and provide examples for equation matching.

Pre-estimation of Trajectories and Their Derivatives The equation matching framework requires estimating  $\frac{d\mathbf{X}}{dt}, \dots, \frac{d^K\mathbf{X}}{dt^K}$  from the observed data  $Y_{ij}$ . This can usually be accomplished using RKHS regression, as in Dai and Li (2022). Specifically, estimators for  $\mathbf{X}$ , denoted as  $\hat{\mathbf{X}} = (\hat{X}_1, \dots, \hat{X}_p)^{\mathsf{T}}$ , can be obtained by solving:

$$\hat{X}_{i} = \arg\min_{f \in \mathcal{H}(\mathcal{K})} \left\{ \frac{1}{n} \sum_{j=1}^{n} \left( Y_{ij} - f(t_{j}) \right)^{2} + \nu_{i} \| Pf \|_{\mathcal{H}}^{2} \right\}$$
 (7)

for i = 1, ..., p, where P denotes a penalization operator from  $\mathcal{H}$  to  $\mathcal{H}$ , and  $\nu_i$  is a tuning parameter that controls the strength of regularization. When  $\operatorname{Ker}(P)$  is a finite-dimensional space, the solution to (7) with  $\nu_i > 0$  is unique and can be computed through a finite-dimensional optimization problem (Hsing and Eubank, 2015). The tuning parameters  $\nu_i$  can be selected using generalized cross-validation (GCV); see Section 3.2.2 of Gu and Gu (2013) for details.

One typical RKHS is the Sobolev space:

$$\mathcal{W}_q(\mathcal{T}) := \left\{ f \in L^2([0, C]) \middle| \frac{\mathrm{d}^q f}{\mathrm{d} t^q} \text{ exists and } \frac{\mathrm{d}^q f}{\mathrm{d} t^q} \in L^2([0, C]) \right\}$$

where the reproducing kernel is  $\mathcal{K}(t,s) := \sum_{l=0}^{q-1} \frac{t^l}{l!} \frac{s^l}{l!} + \int_0^C \frac{(t-u)_+^{q-1}}{(q-1)!} \frac{(s-u)_+^{q-1}}{(q-1)!} du$  for  $q \geq 1$ , and

 $\mathcal{T} = [0, C]$ . Sobolev space is a common functional space used for estimating latent smooth trajectories from noisy observations (Gu and Gu, 2013; Hsing and Eubank, 2015; Tan, Shi and Zhang, 2024). When adopting the functional space, we require that  $q \leq K$  as X is only known to be K-times differentiable based on (3). A larger value of q may be used if  $f_i(X(t), t)$  is further differentiable with respect to t.

To penalize functions in Sobolev space, we specifically focus on the penalty  $||Pf||_{\mathcal{H}}^2 = \left\|\frac{\mathrm{d}^q f}{\mathrm{d}t^q}\right\|_{L^2}^2$ , which regulates the roughness of the q-th order derivative of the curve. Under this penalty, (7) can be solved using penalized spline regression (Wahba, 1990).

Equation Matching with Denoised Trajectories With the pre-estimated trajectories, we obtain the empirical loss for equation matching based on (6):

$$\int_{0}^{C} \left\| \mathcal{F}_{f,\omega} \left( \hat{\boldsymbol{X}}, \frac{\mathrm{d}\hat{\boldsymbol{X}}}{\mathrm{d}t}, \cdots, \frac{\mathrm{d}^{K}\hat{\boldsymbol{X}}}{\mathrm{d}t^{K}}, t \right) \right\|^{2} \nu(t) \, \mathrm{d}t.$$
 (8)

This loss is then used to estimate f and  $\omega$  from the pre-estimated trajectories.

A common issue with the above procedure is its possible reliance on estimated highorder derivatives. Although  $\frac{\mathrm{d}^l \hat{X}}{\mathrm{d}t^l}$  for l > 0 is an estimator for  $\frac{\mathrm{d}^l X}{\mathrm{d}t^l}$ , its statistical convergence behavior tends to deteriorate as the order l increases (Cox, 1983). This phenomenon is illustrated in Figure 1 using simulated data examples, which show that high-order derivatives are inaccurately estimated from the noisy data. These inaccuracies highlight the importance of constructing  $\mathcal{F}_{f,\omega}(\cdot)$  in a way that avoids dependence on high-order derivatives.

**Examples of Matching Operators** We connect two important equation discovery methods to our equation matching framework, each corresponding to a different construction of the matching operator  $\mathcal{F}_{f,\omega}(\cdot)$ .

Let  $\mathcal{F}_{f,\omega}^i(\cdot)$  be the *i*-th component of  $\mathcal{F}_{f,\omega}(\cdot)$ . An operator  $\mathcal{F}_{f,\omega}^i$  directly induced by (3)

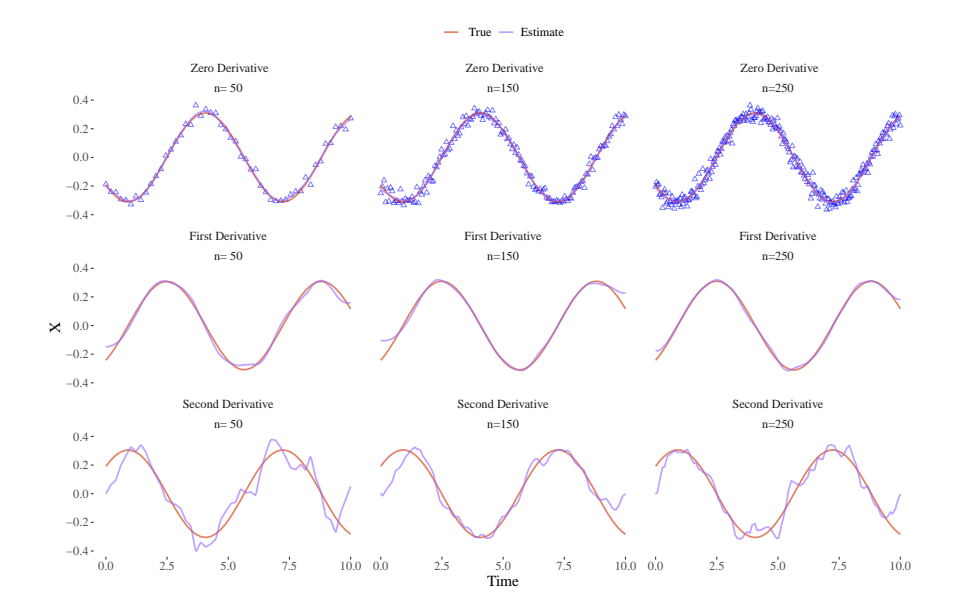


Figure 1: The true trajectories and their derivatives, along with the corresponding estimates obtained from noisy observations using RKHS regressions. In these examples, the signal-to-noise ratio is set to 0.15, and the sample sizes n = 50, 150, 250, with observation points evenly spaced over the time interval [0, 10]. The blue triangles denote the observed data points.

is given by

$$\mathcal{F}_{\boldsymbol{f},\boldsymbol{\omega}}^{i}\left(\boldsymbol{X},\frac{\mathrm{d}\boldsymbol{X}(t)}{\mathrm{d}t},\cdots,\frac{\mathrm{d}^{K}\boldsymbol{X}(t)}{\mathrm{d}t^{K}},t\right) = \frac{\mathrm{d}^{K}X_{i}(t)}{\mathrm{d}t^{K}} + \sum_{l=1}^{K-1} w_{il}\frac{\mathrm{d}^{l}X_{i}(t)}{\mathrm{d}t^{l}} - f_{i}(\boldsymbol{X}(t),t),$$
(9)

where the equation matching becomes a regression of the gradients

$$\frac{\mathrm{d}^{K}X_{i}(t)}{\mathrm{d}t^{K}} + \sum_{l=1}^{K-1} w_{il} \frac{\mathrm{d}^{l}X_{i}(t)}{\mathrm{d}t^{l}}$$

onto X(t) and t,  $\forall t \in [0, C]$ . One well-known gradient-based method is sparse identification of nonlinear dynamics (SINDy; Brunton et al., 2016), which applies sparse regression to recover governing equations from data by exploiting parsimony structures of dynamical systems. Several extensions of SINDy have since been proposed to enhance its performance and broaden its applicability (Kaiser et al., 2018; Champion et al., 2019; Fasel et al., 2022; Egan et al., 2024).

An alternative approach for equation discovery is established using the Newton-Leibniz

formula, which transforms the differential equation (3) into an integral equation (Chen et al., 2017; Schaeffer and McCalla, 2017; Dai and Li, 2022). Specifically, we integrate both sides of the original ordinary differential equation and yield:

$$\frac{\mathrm{d}^{K-1}X_i}{\mathrm{d}t^{K-1}}(t) + \sum_{l=1}^{K-1} \omega_{il} \frac{\mathrm{d}^{l-1}X_i}{\mathrm{d}t^{l-1}}(t) = \alpha_i + \int_0^t f_i(\mathbf{X}(s), s) \,\mathrm{d}s,$$

where  $\alpha_i$  is an additional scalar parameter. Given this, the matching operator is constructed as

$$\mathcal{F}_{\boldsymbol{f},\boldsymbol{\omega},\alpha_{i}}^{i}\left(\boldsymbol{X},\frac{\mathrm{d}\boldsymbol{X}(t)}{\mathrm{d}t},\cdots,\frac{\mathrm{d}^{K-1}\boldsymbol{X}(t)}{\mathrm{d}t^{K-1}},t\right)$$

$$=\frac{\mathrm{d}^{K-1}X_{i}(t)}{\mathrm{d}t^{K-1}}+\sum_{l=1}^{K-1}\omega_{il}\frac{\mathrm{d}^{l-1}X_{i}(t)}{\mathrm{d}t^{l-1}}-\alpha_{i}-\int_{0}^{t}f_{i}(\boldsymbol{X}(s),s)\mathrm{d}s.$$
(10)

The equation matching with (10) is referred to as integral matching (Ramsay and Hooker, 2017; Dattner and Klaassen, 2015). In contrast to (9), integral matching introduces auxiliary parameters  $\alpha_i$  to eliminate dependence on the highest-order derivative  $\frac{d^K \mathbf{X}}{dt^K}$ .

In the special case of first-order dynamics (K = 1), integral matching completely avoids the need for derivative estimation. However, for higher-order dynamics (K > 1), direct integration as described above does not entirely eliminate the necessity of estimating derivatives of the underlying trajectories. This may introduce inaccuracies in equation matching for general-order systems.

### 2.2 Equation Matching with Green's Functions

In this section, we unify gradient matching and integral matching within a common framework—termed general-order equation matching—by using the Green's function of differential operators. Formally, let  $\mathcal{P}$  be a differential operator defined on functions over the interval [0, C]. The Green's function associated with  $\mathcal{P}$  is a bivariate kernel function G(t, s) defined on  $[0, C]^2$ , which satisfies

$$\mathcal{P}G(t,s) = \delta(t-s),\tag{11}$$

where  $\mathcal{P}$  is applied to the variable t. Given G(t,s), the solution X(t) to  $\mathcal{P}X(t)=f(t)$  can be written as

$$X(t) = g(t) + \int_0^C G(t, s) f(s) ds,$$

where g is any function from  $Ker(\mathcal{P})$ . In this context, the Green's function acts as an inverse of the operator  $\mathcal{P}$ , providing a way to reduce the differential order and represent solutions in an integral form.

When  $\mathcal{P}$  is the k-th order derivative operator  $\frac{d^k}{dt^k}$ , the corresponding Green's function can be explicitly given by:

$$G^{k}(t,s) = \frac{(t-s)^{k-1}}{(k-1)!} \mathbb{I}(t \ge s), \quad k \ge 1.$$
(12)

This equation can be directly verified by the definition of Green's function. For k = 0, we similarly define the zero-order Green's function as  $G^0(t,s) = \delta(t-s)$ , corresponding to the case where  $\mathcal{P}$  is the identical operator. In the following, we apply these Green's functions to reduce the order of the differential equation (3); see the next theorem.

**Theorem 1** (Integral Form of Differential Equations). Given any integer k such that  $1 \le k \le K - 1$ , the differential equation (3) is equivalent to the following integral equation:

$$\frac{\mathrm{d}^{K-k}X_{i}}{\mathrm{d}t^{K-k}}(t) + \sum_{l=k+1}^{K-1} \omega_{il} \frac{\mathrm{d}^{l-k}X_{i}}{\mathrm{d}t^{l-k}}(t) + \sum_{l=1}^{\min(k,K-1)} \omega_{il} \cdot \int_{0}^{C} G^{k-l}(t,s)X_{i}(s) \,\mathrm{d}s$$

$$= g_{ik}(t) + \int_{0}^{C} G^{k}(t,s)f_{i}(\boldsymbol{X}(s),s) \,\mathrm{d}s, \tag{13}$$

where  $g_{ik}$  is a function from Ker  $\left(\frac{\mathrm{d}^k}{\mathrm{d}t^k}\right)$ . For k > K, we replace the term  $\frac{\mathrm{d}^{K-k}X_i}{\mathrm{d}t^{K-k}}(t)$  in (13) with its integral counterpart  $\int_0^C G^{k-K}(t,s)X_i(s)\,\mathrm{d}s$ . When  $k \geq K-1$ , we remove the term  $\sum_{l=k+1}^{K-1} \omega_{il} \frac{\mathrm{d}^{l-k}X_i}{\mathrm{d}t^{l-k}}(t)$  from (13). Similarly, we remove the term  $\sum_{l=1}^{\min(k,K-1)} \omega_{il} \int_0^C G^{k-l}(t,s)X_i(s)\,\mathrm{d}s$  when k=0.

Theorem 1 generalizes the equation (12) in Tan, Zhang, Wang, Huang and Yao (2024) to integral equations of arbitrary order, which can be obtained by applying the Green's function of the differential operator  $\frac{d^k}{dt^k}$  to both sides of (3). When k = 0 and k = 1, this becomes the original differential equation (3) and its Newton-Leibniz integral form, respectively. By increasing k beyond 1, and even beyond the true order K, we obtain an equivalent integral equation only involving derivatives of lower order.

Based on equation (13), we define the corresponding equation matching procedure as follows.

**Definition 1** (Order-k Equation Matching). For  $k \geq 0$ , define the matching operator  $\mathcal{F}_{f,\omega,g_{ik}}^{i}$  according to (13):

$$\mathcal{F}_{f,\omega,g_{ik}}^{i}\left(\boldsymbol{X},\frac{\mathrm{d}\boldsymbol{X}}{\mathrm{d}t},\dots,\frac{\mathrm{d}^{K-k}\boldsymbol{X}}{\mathrm{d}t^{K-k}},t\right) := \frac{\mathrm{d}^{K-k}X_{i}}{\mathrm{d}t^{K-k}}(t) +$$

$$\sum_{l=k+1}^{K-1} \omega_{il} \frac{\mathrm{d}^{l-k}X_{i}}{\mathrm{d}t^{l-k}}(t) + \sum_{l=1}^{\min(k,K-1)} \omega_{il} \int_{0}^{C} G^{k-l}(t,s)X_{i}(s) \,\mathrm{d}s - g_{ik}(t) - \int_{0}^{C} G^{k}(t,s)f_{i}(\boldsymbol{X}(s),s) \,\mathrm{d}s.$$
(14)

The corresponding loss is defined as

$$\int_{0}^{C} \sum_{i=1}^{p} \left| \mathcal{F}_{f,\boldsymbol{\omega},g_{ik}}^{i} \left( \boldsymbol{X}, \frac{\mathrm{d}\boldsymbol{X}}{\mathrm{d}t}, \dots, \frac{\mathrm{d}^{K-k}\boldsymbol{X}}{\mathrm{d}t^{K-k}}, t \right) \right|^{2} \nu(t) \, \mathrm{d}t.$$
 (15)

We refer to the equation matching based on this loss as order-k equation matching.

**Remark 1** (Connections to Gradient- and Integral-Based Methods for Equation Discovery). The loss function (15) unifies two commonly used techniques: integral matching when k = 1,

and gradient matching when k=0. For  $k\geq 2$ , the order-k equation matching depends only on the estimated state  $\hat{X}$  and its lower-order derivatives  $\left\{\frac{\mathrm{d}^l\hat{X}}{\mathrm{d}t^l}\right\}_{1\leq l\leq K-k}$ , providing an equation discovery framework that is less dependent on high-order derivatives.

Remark 2 (Derivative-Free Equation). Note that when  $k \geq K$ , all derivatives are eliminated from the loss (15); however, the dimension of the space  $\operatorname{Ker}\left(\frac{\mathrm{d}^k}{\mathrm{d}t^k}\right)$  associated with  $g_{ik}$  increases with k, introducing greater model complexity for equation discovery. A suitable choice is k = K, which yields derivative-free equation matching with minimal model complexity. We focus on this type of equation matching in the following sections.

# 3 Sparse Equation Matching

Since no parametric form is assumed for the underlying dynamical system, we cannot directly use (15) to estimate the driving function f from denoised trajectories. To address this issue, we extend the sparse equation discovery framework in Brunton et al. (2016) to our equation matching framework, which involves constructing a candidate set of basis functions of X to provide a prior structure for the dynamical system.

Specifically, we define

$$\boldsymbol{H}: \mathbb{R}^{p+1} \to \mathbb{R}^{D}, \quad (\boldsymbol{X}^{\top}(t), t)^{\top} \mapsto \boldsymbol{H}(\boldsymbol{X}(t), t) \quad \forall, \ t \in [0, C],$$

where  $\boldsymbol{H}(\cdot)$  consists of D basis functions to capture the dynamic of the differential equations. To simplify the notation, we denote  $(\boldsymbol{X}^{\top}(t),t)^{\top}$  as  $\boldsymbol{X}(t)$  by treating the time as a state variable. Under this, we assume that  $f_i$  in (3) admits the following decomposition:

$$f_i(\mathbf{X}(t)) = \mathbf{H}^{\top}(\mathbf{X}(t))\boldsymbol{\beta}_i, \tag{16}$$

where  $\boldsymbol{\beta}_i = (\beta_{i1}, \dots, \beta_{iD})^{\top}$  is a *D*-dimensional coefficient vector that captures the contribution of each basis function. We suppose that  $\boldsymbol{\beta}_i$  is sparse, i.e., it contains only a small number of nonzero entries. This reflects the parsimonious structure of dynamical systems assumed in the literature (Brunton et al., 2016; Chen et al., 2017; Fasel et al., 2022).

Several strategies can be considered for the construction of  $\mathbf{H}(\cdot)$ . A common approach involves constructing candidate terms based on polynomial and trigonometric functions (Brunton et al., 2016; Zhang et al., 2020; Brunton and Kutz, 2022) — functional forms that arise from Taylor and Fourier representations of governing physical laws. Specifically,  $\mathbf{H}(\mathbf{X}(t))$  can be taken as a subset of the following candidate basis functions:

$$(1, \sin(\boldsymbol{X}), \cos(\boldsymbol{X}), \boldsymbol{X}, \boldsymbol{X}^2, \dots, \boldsymbol{X}^P)^\top,$$
 (17)

which consists of constant term, trigonometric terms  $\sin(\mathbf{X})$ ,  $\cos(\mathbf{X})$ , and polynomial terms  $\mathbf{X}, \mathbf{X}^2, \dots, \mathbf{X}^P$ , where  $\mathbf{X}^P$  denote the vector of all polynomials of the components of  $\mathbf{X}$  up to degree P, that is,

$$\mathbf{X}^{P} = (X_{1}^{P}, X_{1}^{P-1} X_{2} \dots, X_{p-1} X_{p}^{P-1}, X_{p}^{P}).$$

Moreover, one may construct an RKHS-based model for  $f_i$  using the additive structure, where each additive component is assumed to lie in an RKHS; see Dai and Li (2022) for the details. In this work, we focus on the first framework in (17) for constructing  $\mathbf{H}(\cdot)$ .

Remark 3 (Connections to Network Discovery of Dynamical Systems). Model (16) provides a meaningful interpretation for the task of network discovery in dynamical systems, which aims to identify the underlying interactions among system components—often represented as a directed graph on the system components (Friston et al., 2003; Kiebel et al., 2009; Chen et al., 2017). Through a sparse estimation of  $\beta_i$  in (16), we enables the network discovery by

expressing the dynamics through a system of equations governed by a set of basis functions. For example, if some of the coefficients corresponding to basis functions involving  $X_k$  are nonzero, then  $X_k$  influences the dynamics of  $X_i$ . We then construct a directed edge from  $X_k$  to represent this influence in the system, capturing mechanisms such as regulation or information flow in the network.

According to (14), we apply the order-K equation matching equipped with the construction in (16). This yields the following matching operator:

$$\mathcal{F}_{\boldsymbol{\theta}_{i},g_{iK}}^{i}(\boldsymbol{X},t) := X_{i}(t) + \left(\int_{0}^{C} G^{K-1}(t,s)X_{i}(s)\mathrm{d}s, \dots, \int_{0}^{C} G(t,s)X_{i}(s)\mathrm{d}s\right)\boldsymbol{\omega}_{i}$$
$$-\left(\int_{0}^{C} G^{K}(t,s)\boldsymbol{H}^{T}(\boldsymbol{X}(s))\,\mathrm{d}s\right)\boldsymbol{\beta}_{i} - g_{iK}(t), \tag{18}$$

where  $\boldsymbol{\theta}_i := (-\boldsymbol{\omega}_i^{\top}, \boldsymbol{\beta}_i^{\top})^{\top}$  and  $g_{iK} \in \operatorname{Ker}\left(\frac{\mathrm{d}^K}{\mathrm{d}t^K}\right)$ . Let  $\boldsymbol{\Phi}_K(t) = \left(1, t, \dots, t^{K-1}\right)^{\top}$  denote a basis for the null space  $\operatorname{Ker}\left(\frac{\mathrm{d}^K}{\mathrm{d}t^K}\right)$ . Then for any  $g_{iK} \in \operatorname{Ker}\left(\frac{\mathrm{d}^K}{\mathrm{d}t^K}\right)$ , it can be expressed as  $g_{iK}(t) = \boldsymbol{\Phi}_K^{\top}(t)\boldsymbol{\alpha}_i$  for some  $\boldsymbol{\alpha}_i \in \mathbb{R}^K$ . Due to this, we denote  $\mathcal{F}_{\boldsymbol{\theta}_i,g_{iK}}^i$  by  $\mathcal{F}_{\boldsymbol{\theta}_i,\boldsymbol{\alpha}_i}^i$ .

Define

$$\Theta_i(\boldsymbol{X}(t)) := \left( \int_0^C \boldsymbol{G}^{K-1}(t,s) X_i(s) \mathrm{d}s, \int_0^C G^K(t,s) \boldsymbol{H}^\top(\boldsymbol{X}(s)) \, \mathrm{d}s \right),$$
with 
$$\int_0^C \boldsymbol{G}^{K-1}(t,s) X_i(s) \mathrm{d}s := \left( \int_0^C G^{K-1}(t,s) X_i(s) \mathrm{d}s, \dots, \int_0^C G(t,s) X_i(s) \mathrm{d}s \right).$$

The first block  $\int_0^C \mathbf{G}^{K-1}(t,s)X_i(s)\mathrm{d}s$  in  $\mathbf{\Theta}_i(\mathbf{X}(t))$  corresponds to terms from the differential operator in (3), while the remaining  $\int_0^C G^K(t,s) \mathbf{H}^{\top}(\mathbf{X}(s)) \mathrm{d}s$  corresponds to terms from the driving function  $f_i$ . We then have

$$\mathcal{F}_{\boldsymbol{\theta}_{i},\boldsymbol{\alpha}_{i}}^{i}(\boldsymbol{X},t) = X_{i}(t) - \boldsymbol{\Theta}_{i}(\boldsymbol{X}(t))\boldsymbol{\theta}_{i} - \boldsymbol{\Phi}_{K}^{\top}(t)\boldsymbol{\alpha}_{i}.$$
(19)

Similar to  $\beta_i$ , we assume that  $\theta_i$  is a sparse vector for each i. This enables parsimonious

equation discovery for both the linear differential operator and the driving function in (3), providing flexibility in uncovering the governing equations of general-order systems.

To facilitate the sparse estimation, we estimate  $\theta_i$  and  $\alpha_i$  by minimizing a regularized equation matching loss:

$$(\hat{\boldsymbol{\theta}}_{i}, \hat{\boldsymbol{\alpha}}_{i}) = \arg \min_{\boldsymbol{\theta}_{i} \in \mathbb{R}^{K-1+D}, \boldsymbol{\alpha}_{i} \in \mathbb{R}^{K}} \mathcal{L}_{i}(\boldsymbol{\theta}_{i}, \boldsymbol{\alpha}_{i} \mid \boldsymbol{X})$$

$$:= \arg \min_{\boldsymbol{\theta}_{i} \in \mathbb{R}^{K-1+D}, \boldsymbol{\alpha}_{i} \in \mathbb{R}^{K}} \int_{0}^{C} \left| \mathcal{F}_{\boldsymbol{\theta}_{i}, \boldsymbol{\alpha}_{i}}^{i}(\boldsymbol{X}, t) \right|^{2} dt + R(\boldsymbol{\theta}_{i}), \tag{20}$$

where  $R(\boldsymbol{\theta}_i)$  is a sparsity-inducing penalty applied to  $\boldsymbol{\theta}_i$ , i = 1, ..., p. We approximate the integral in (20) on dense discrete time grids. Then the minimization of (20) is then a standard sparse least squares regression problem.

To enforce sparsity, one may apply the least absolute shrinkage and selection operator (LASSO) penalty (Hastie et al., 2017), i.e.,  $R(\boldsymbol{\theta}_i) = \lambda_i \|\boldsymbol{\theta}_i\|_1$ , where  $\|\boldsymbol{\theta}_i\|_1$  is the  $\ell_1$ -norm of  $\boldsymbol{\theta}_i$  and  $\lambda_i$  is a tuning parameter. This penalty has been widely adopted in the context of equation discovery (Champion et al., 2019; Brunton and Kutz, 2022; Egan et al., 2024). Other sparse regression techniques, such as the elastic net (Zou and Hastie, 2005), group LASSO (Yuan and Lin, 2006), and adaptive best-subset selection (ABESS) (Zhu et al., 2020), may also be employed for the equation matching.

We refer to the regularized formulation in (20) as sparse equation matching (SEM). The complete SEM procedure is outlined in Algorithm 1.

For SEM with the LASSO penalty  $R(\boldsymbol{\theta}_i) = \lambda_i \|\boldsymbol{\theta}_i\|_1$ , the tuning parameter  $\lambda_i$  is selected via 10-folds cross-validation (CV) for each i. Specifically, we partition the time interval [0, C] evenly into ten disjoint subintervals  $\{I_l\}_{l=1}^{10}$ . Let  $\hat{\boldsymbol{X}}$  denote the estimated trajectories obtained from (7). Given a fixed value of  $\lambda_i$ , the l-fold-specific estimates  $(\hat{\boldsymbol{\theta}}_i^{(l)}, \hat{\boldsymbol{\alpha}}_i^{(l)})$  are

#### Algorithm 1 Sparse Equation Matching for General-Order Dynamical Systems

1: **Input**: Observed time points  $t_j$ , j = 1, ..., n; noisy observations  $Y_i(t_j)$ , i = 1, ..., p, j = 1, ..., n; order q of the Sobolev space; D fixed candidate basis functions  $\mathbf{H}(\cdot)$ ; sparsity-inducing penalty  $R(\cdot)$ .

2: **for** i = 1, ..., p **do** 

3: Estimate the trajectory  $\hat{X}_i(t)$  by solving:

$$\hat{X}_i = \arg\min_{f \in \mathcal{W}_q(\mathcal{T})} \left\{ \frac{1}{n} \sum_{j=1}^n \left( Y_{ij} - f(t_j) \right)^2 + \nu_i \left\| \frac{\mathrm{d}^q f}{\mathrm{d} t^q} \right\|_{L^2}^2 \right\},\,$$

where  $\nu_i$  is chosen via GCV.

4: end for

5: Construct the full trajectory  $\hat{\boldsymbol{X}}(t) = (\hat{X}_1(t), \dots, \hat{X}_p(t))^{\top}$ .

6: **for** i = 1, ..., p **do** 

7: Given  $t \in [0, C]$ , calculate  $\Phi_K(t) = (1, t, \dots, t^{K-1})^{\top}$  and

$$\boldsymbol{\Theta}_i(\hat{\boldsymbol{X}}(t)) := \left( \int_0^C \boldsymbol{G}^{K-1}(t,s) \hat{X}_i(s) \, \mathrm{d}s, \right.$$
$$\left. \int_0^C G^K(t,s) \boldsymbol{H}^\top(\hat{\boldsymbol{X}}(s)) \, \mathrm{d}s \right).$$

8: Estimate coefficients by solving the regularized equation-matching problem:

$$(\hat{\boldsymbol{\theta}}_i, \hat{\boldsymbol{\alpha}}_i) = \arg\min_{\boldsymbol{\theta}_i, \boldsymbol{\alpha}_i} \int_0^C \left| \hat{X}_i(t) - \boldsymbol{\Theta}_i(\hat{\boldsymbol{X}}(t)) \boldsymbol{\theta}_i - \boldsymbol{\Phi}_K^{\top}(t) \boldsymbol{\alpha}_i \right|^2 \mathrm{d}t + R(\boldsymbol{\theta}_i).$$

9: end for

10: Output:  $\hat{\boldsymbol{\theta}}_i$ ,  $\hat{\boldsymbol{\alpha}}_i$  for  $i = 1, \dots, p$ .

obtained by solving:

$$\left(\hat{\boldsymbol{\theta}}_{i}^{(l)}, \hat{\boldsymbol{\alpha}}_{i}^{(l)}\right) = \arg\min_{\boldsymbol{\theta}_{i}, \boldsymbol{\alpha}_{i}} \left\{ \int_{0}^{C} \left| \mathcal{F}_{\boldsymbol{\theta}_{i}, \boldsymbol{\alpha}_{i}}^{i}(\hat{\boldsymbol{X}}, t) \right|^{2} \mathbb{I}(t \notin I_{l}) dt + \lambda_{i} \|\boldsymbol{\theta}_{i}\|_{1} \right\}.$$

The cross-validation error for  $\lambda_i$  is then computed as:

$$CV(\lambda_i) := \frac{1}{10} \sum_{l=1}^{10} \left( \int_0^C \left| \mathcal{F}_{\hat{\boldsymbol{\theta}}_i^{(l)}, \hat{\boldsymbol{\alpha}}_i^{(l)}}^i(\hat{\boldsymbol{X}}, t) \right|^2 \mathbb{I}(t \in I_l) dt \right).$$

Similar to (20), we approximate the above integral on dense discrete time grids. The optimal tuning parameter is then selected by minimizing the cross-validation error.

Remark 4 (Invariance of Sparse Equation Matching). Note that any function of the form

$$\tilde{G}^k(t,s) = G^k(t,s) + \mathbf{\Phi}_k^{\top}(t)\mathbf{v}_k(s)$$

is also a valid Green's function for the differential operator  $\frac{d^k}{dt^k}$ , where  $\boldsymbol{\Phi}_k(t) := (1, t, \dots, t^{k-1})^{\top}$  denote a basis for Ker  $\left(\frac{d^k}{dt^k}\right)$  and  $\boldsymbol{v}_k(s) := (\psi_{k1}(s), \dots, \psi_{kk}(s))^{\top}$  is an arbitrary function from [0, C] to  $\mathbb{R}^k$ . The following result shows that the estimation of  $\boldsymbol{\theta}_i$  is invariant to the choice of Green's functions.

**Theorem 2** (Invariance of SEM Estimation to Green's Function Choice). Let  $\tilde{G}^k$  be any valid Green's function for the differential operator  $\frac{\mathrm{d}^k}{\mathrm{d}t^k}$ . Given any regularization function  $R(\cdot)$  and a set of basis functions  $H(\cdot)$ , define the equation-matching operator associated with  $\{\tilde{G}^k\}_{k=1}^K$  as:

$$\tilde{\mathcal{F}}_{\boldsymbol{\theta}_i, \boldsymbol{\alpha}_i}^i(\boldsymbol{X}, t) = X_i(t) - \tilde{\boldsymbol{\Theta}}_i(\boldsymbol{X}(t))\boldsymbol{\theta}_i - \boldsymbol{\Phi}_K^{\top}(t)\boldsymbol{\alpha}_i,$$

where  $\tilde{\boldsymbol{\Theta}}_i(\boldsymbol{X}(t))$  is given by

$$\tilde{\boldsymbol{\Theta}}_i(\boldsymbol{X}(t)) := \left( \int_0^C \tilde{G}^{K-1}(t,s) X_i(s) \, \mathrm{d}s, \ \dots, \ \int_0^C \tilde{G}(t,s) X_i(s) \, \mathrm{d}s, \ \int_0^C \tilde{G}^K(t,s) \boldsymbol{H}^\top(\boldsymbol{X}(s)) \, \mathrm{d}s \right).$$

The corresponding SEM estimator is defined as

$$(\tilde{\boldsymbol{\theta}}_i, \tilde{\boldsymbol{\alpha}}_i) := \arg\min_{\boldsymbol{\theta}_i \in \mathbb{R}^{K-1+D}, \boldsymbol{\alpha}_i \in \mathbb{R}^K} \int_0^C \left| \tilde{\mathcal{F}}_{\boldsymbol{\theta}_i, \boldsymbol{\alpha}_i}^i(\boldsymbol{X}, t) \right|^2 \mathrm{d}t + R(\boldsymbol{\theta}_i).$$

Let  $\tilde{\Theta}$  and  $\tilde{A}$  denote the set of minimizers  $\tilde{\boldsymbol{\theta}}_i$  and  $\tilde{\boldsymbol{\alpha}}_i$  respectively. Denote  $\hat{\Theta}$  and  $\hat{A}$  as the set of corresponding minimizers from (20) using the canonical Green's functions  $\{G^k\}_{k=1}^K$ . Then there exists an identity map id and a bijection  $\mathcal{M}$  such that

$$id(\tilde{\Theta}) = \hat{\Theta}, \text{ and } \mathcal{M}(\tilde{\mathcal{A}}) = \hat{\mathcal{A}}.$$

Theorem 2 indicates that different choices of Green's functions only affect the null space component  $g_{iK}$  in (18), but do not alter the SEM estimates  $\hat{\boldsymbol{\theta}}_i$ .

### 4 Simulation

In this section, we assess the numerical performance of SEM with the LASSO penalty. We compare our method with a gradient-based approach equipped with the LASSO penalty—SINDy (Brunton et al., 2016)—which corresponds to order-0 sparse equation matching.

We compare the above two methods using two examples of second-order ODEs. For each example, we first numerically simulate the trajectories  $X_i$ ,  $i=1,\ldots,p$ , on an evenly spaced time grid  $\{t_j; j=1,\ldots,n\}$  over the interval [0,C]. We then generate observations  $Y_i(t_j)$  from a normal distribution with mean  $X_i(t_j)$  and variance  $\sigma_i^2$ , where  $\sigma_i^2 = \gamma^2 \int_0^C X_i^2(t) \, dt/C$ , and  $\gamma$  controls the noise level. For comparison, both methods are implemented using the same pre-estimation procedure based on RKHS regression (7), with  $\mathcal{H}(\mathcal{K}) = \mathcal{W}_2(\mathcal{T})$  and penalty term  $\|Pf\|_{\mathcal{H}}^2 = \left\|\frac{\mathrm{d}^q f}{\mathrm{d}t^q}\right\|_{L^2}^2$ ; the tuning parameter is selected via GCV. In all cases, we consider sample sizes n=50,150,250,350, evenly spaced in [0,C], and noise levels  $\gamma=0.05,0.07,0.09$ . Each experiment is repeated 500 times.

In the following, we demonstrate each example of ODEs separately.

Nonlinear Pendulum The nonlinear pendulum equation describes the motion of a single pendulum that swings under the influence of gravity, serving as a fundamental example of a nonlinear differential equation in classical mechanics (Hairer et al., 2006; Thompson and Stewart, 2002). The equation is given by:

$$\frac{\mathrm{d}^2 X(t)}{\mathrm{d}t^2} = -\sin(X(t)),$$

where X(t) represents the angular displacement of the pendulum at time t. We numerically solve the nonlinear pendulum system on the interval [0,20], with initial conditions  $(X(0), \frac{\mathrm{d}X(0)}{\mathrm{d}t})$  sampled from the uniform distribution  $\mathrm{U}([-0.5,0.5]^2)$ . In this case, we set  $\boldsymbol{H}(X) = (1,X,X^2,X^3,X^4,\sin(X),\cos(X))^{\mathrm{T}}$  for equation discovery.

We evaluate the performance of equation discovery using the relative error rate (RER), defined by:

RER := 
$$\frac{1}{S} \sum_{s=1}^{S} \frac{\|\hat{f}^s - f\|_2}{\|f\|_2}$$
,

where  $f(\cdot)$  is the true driving function of an ODE,  $\hat{f}^s(\cdot)$  is the estimated driving function in the s-th replicated experiment, and S is the number of replicated simulations. The RERs of the nonlinear pendulum with S = 500 and various values of n's and  $\gamma$ 's are shown in Figure 2 (A). We observe that SEM consistently outperforms SINDy across all tested values of n and  $\gamma$ . The suboptimal performance of SINDy may stem from inaccuracies in the estimation of derivatives, which introduce substantial errors into the equation discovery process and compromise the fidelity of the discovered models.

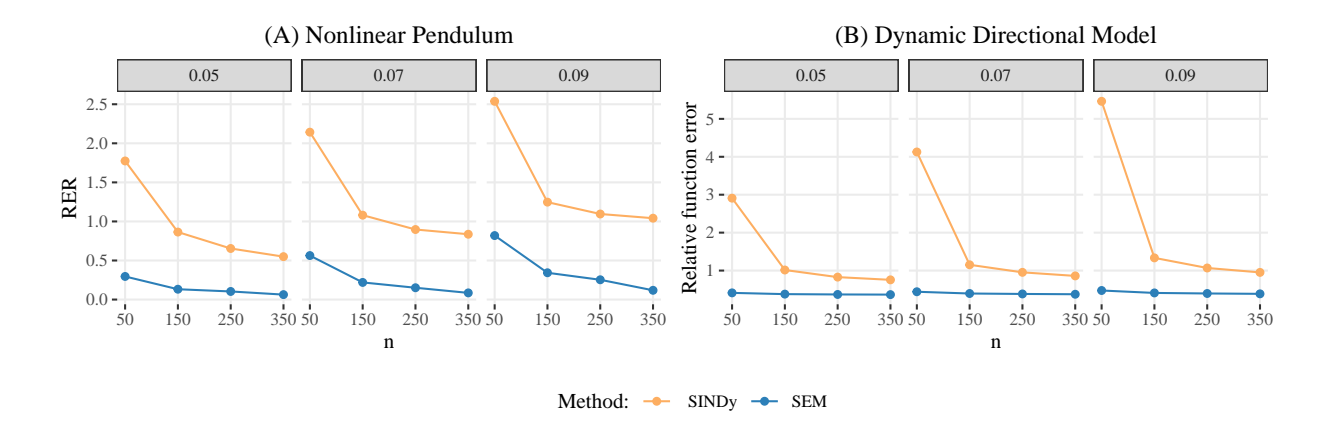


Figure 2: Relative error rate (RER) of the estimated driving functions under various sample sizes n and contamination levels  $\gamma$  (main title of each subgraph).

To illustrate the behavior of equation discovery, we plot the vector fields corresponding to both the true and discovered dynamics of the nonlinear pendulum. The vector field  $\mathcal{F}$  is

defined by the mapping:

$$\mathcal{F}: \left(X(t), \frac{\mathrm{d}X(t)}{\mathrm{d}t}\right) \mapsto \left(\frac{\mathrm{d}X(t)}{\mathrm{d}t}, f\left(X(t), \frac{\mathrm{d}X(t)}{\mathrm{d}t}\right)\right),$$

where  $\left(X(t), \frac{\mathrm{d}X(t)}{\mathrm{d}t}\right)$  represents an arbitrary input location and velocity of the trajectory, f denotes a function of X(t) and  $\frac{\mathrm{d}X(t)}{\mathrm{d}t}$  for modeling the second-order derivatives (i.e., acceleration), and  $\left(\frac{\mathrm{d}X(t)}{\mathrm{d}t}, f\left(X(t), \frac{\mathrm{d}X(t)}{\mathrm{d}t}\right)\right)$  is the output derivative of the location and velocity—that is, the velocity and acceleration of the system. The function f is determined either by the true differential equation (e.g.,  $f\left(X(t), \frac{\mathrm{d}X(t)}{\mathrm{d}t}\right) = \sin(X(t))$ ) or by an equation discovered using different methods. The resulting mapping produces an array of arrows at each point in the plane of  $\mathbb{R}^2$ , indicating both magnitude and direction that visually encodes the system dynamics governed by differential equations.

Figure 3 presents both the true vector field and the average of the estimated vector fields for the nonlinear pendulum. These results are computed based on 500 simulation runs under the setting of n = 150 and  $\gamma = 0.05$ . We observe that the vector field estimated using SEM closely approximates the true vector fields, whereas the one obtained via SINDy exhibits noticeable biases.

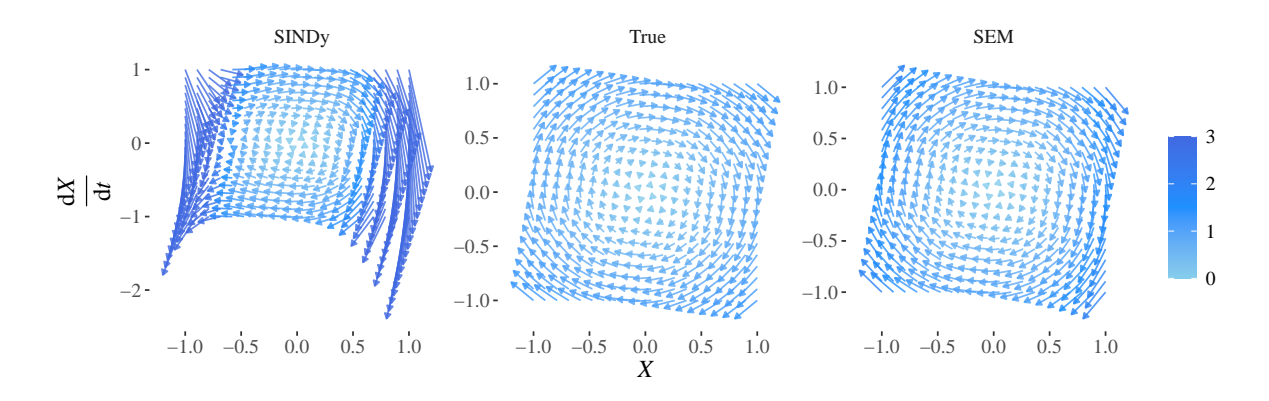


Figure 3: True and average estimated vector fields for the nonlinear pendulum under the setting of n = 150 and  $\gamma = 0.05$ . The color indicates the magnitude of the arrows.

Second-order Dynamic Directional Model Second-order dynamic directional models constitute a fundamental framework for characterizing oscillatory dynamics in neuroscience (Sporns, 2016; Zhang et al., 2020). We consider the following dynamic directional model:

$$\frac{\mathrm{d}^2 X_i(t)}{\mathrm{d}t^2} = a_{1,i} X_i(t) + a_{1,\tau_1(i)} X_{\tau_1(i)}(t) - b_{1,i} \frac{\mathrm{d}X_i(t)}{\mathrm{d}t}, \ i = 1, \dots, \quad 20, 
\frac{\mathrm{d}^2 X_i(t)}{\mathrm{d}t^2} = a_{2,i} X_i(t) + a_{2,\tau_2(i)} X_{\tau_2(i)}(t) - b_{2,i} \frac{\mathrm{d}X_i(t)}{\mathrm{d}t}, \ i = 21, \dots, \quad 40,$$

where  $\tau_1$  is a permutation on  $\{1, 2, ..., 20\}$  and  $\tau_2$  is a permutation on  $\{21, 22, ..., 40\}$ . By this construction, each  $X_i$  can be viewed as a node in a directed network grouped into two clusters, with nodes joined in a directed loop within each cluster. See Figure 9, Panel (A), in Appendix B for an illustration of the directed network structure.

We generate the trajectories of the above dynamic system on the interval [0,5], with the following parameters:

$$a_{1,i} = -4$$
,  $a_{1,\tau_1(i)} = (-1)^i \times 1.2$ ,  $b_{1,i} = -1.3$ ,  $i = 1, \dots, 20$ ,  
 $a_{2,i} = -3.5$ ,  $a_{2,\tau_2(i)} = (-1)^i \times 2$ ,  $b_{2,i} = -2$ ,  $i = 21, \dots, 40$ .

We set the initial conditions as:

$$X_i(0) = 1 - \frac{i-1}{38}, \quad \frac{\mathrm{d}X_i}{\mathrm{d}t}(0) = -1.5 + (-1)^i \times 0.5, \ i = 1, \dots, 20,$$
  
 $X_i(0) = 1.5 - \frac{i-21}{38}, \quad \frac{\mathrm{d}X_i}{\mathrm{d}t}(0) = -1.5 + \frac{2(i-21)}{19}, \ i = 21, \dots, 40.$ 

The generated trajectories are illustrated in Figure 9 (B) in Appendix B. We set  $\boldsymbol{H}(\boldsymbol{X}) = (1, X_1, X_2, \dots, X_{40})^{\top}$  for equation discovery in this case.

We evaluate the performance of equation discovery using the RER, similar to that defined in the nonlinear pendulum example. The RER is given by:

RER := 
$$\frac{1}{p} \sum_{i=1}^{p} \frac{1}{S} \sum_{s=1}^{S} \frac{\|\hat{f}_{i}^{s} - f_{i}\|_{2}}{\|f_{i}\|_{2}},$$

where  $f_i(\cdot)$  is the true driving function for  $X_i$ ,  $\hat{f}_i^s(\cdot)$  is the estimated driving function in the s-th replicated experiment, and S = 500 is the number of replications. The results for the second-order directional dynamic model under varying values of n and  $\gamma$  are shown in Figure 2(B). These findings are consistent with those observed in the nonlinear pendulum example, further demonstrating the advantages of SEM across different dynamical systems.

In the dynamic directional model, we are also interested in identifying the latent directed network, as illustrated in Figure 9 (A) in Appendix B. Specifically, let  $E = \{e_{i,j}\}_{i,j=1}^{40}$  be the adjacency matrix of the true directed network, where  $e_{i,j} = 1$  if  $X_j$  contributes to the change in the second-order derivative of  $X_i$ ; otherwise,  $e_{i,j} = 0$ . To evaluate estimation performance, we similarly define the adjacency matrix  $\hat{E}^s = \{\hat{e}_{i,j}^s\}_{i,j=1}^{40}$  based on the discovered equations in the sth experiment. Accordingly, we define the mean accuracy (MA) as:

$$MA := \frac{1}{S} \sum_{s=1}^{S} \frac{\sum_{i,j=1}^{40} \mathbb{I}(\hat{e}_{i,j}^s = e_{i,j})}{40^2}.$$

In Figure 4, we present the estimation accuracy of the adjacency matrix in the second-order dynamic directional model obtained from the two methods. The results indicate that SEM recovers the network structure more accurately than SINDy.

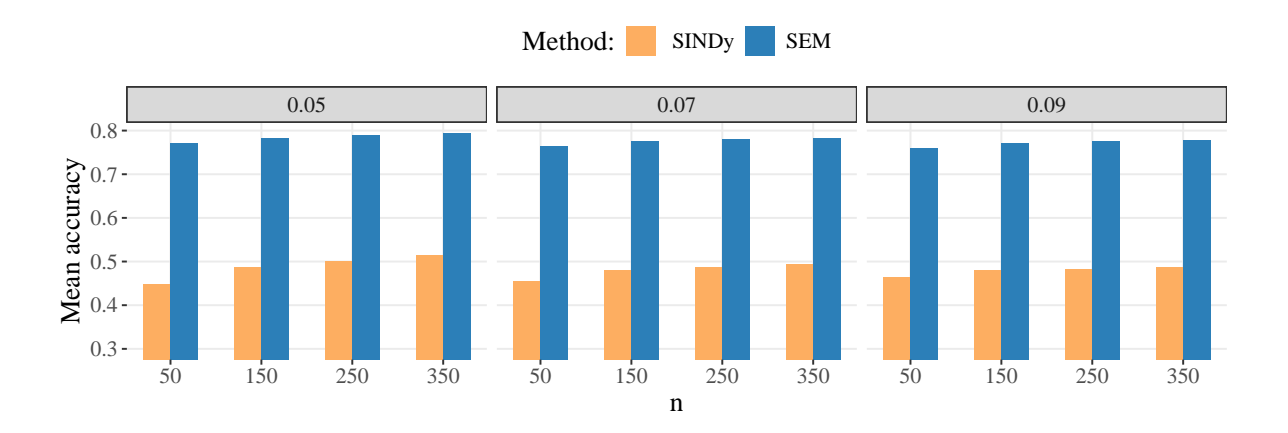


Figure 4: Mean accuracy of the estimated networks under different sample sizes n and noise levels  $\gamma$  (indicated in the title of each subfigure).

To illustrate the behavior of equation discovery, we similarly define the vector field of the dynamic directional model. Take  $X_{19}$  as an example; its vector field is defined as

$$\mathcal{F}_{X_{19}}: \mathbb{R}^2 \to \mathbb{R}^2, \ \left(X_{19}(t), \frac{dX_{19}(t)}{dt}\right) \mapsto \left(\frac{dX_{19}(t)}{dt}, f_{19}\left(X_1(t), \dots, X_{40}(t), \frac{dX_{19}(t)}{dt}\right)\right),$$

where  $f_{19}$  denotes a driving function of  $X_1(t), \ldots, X_{40}(t)$  and  $\frac{\mathrm{d}X_{19}(t)}{\mathrm{d}t}$ , used to model the second-order derivative (acceleration). This function is determined either by the true dynamical equation or by an equation discovered using different methods. To compute  $f_{19}$ , we set  $X_i(t) = b$  for  $i = 1, \ldots, 40$  with  $i \neq 19$ , reflecting the acceleration of  $X_{19}$  conditional on the other trajectories taking the constant value b. In Figure 5, we present both the true vector fields and the means of the estimated vector fields for  $X_{19}$  under three different values of b, based on 500 simulation runs with n = 150 and  $\gamma = 0.05$ . The results show that the vector fields estimated using SEM are more similar to the true fields than those obtained via SINDy.

### 5 Data Analysis

To demonstrate the effectiveness of SEM, we analyze electroencephalogram (EEG) data from a brain–computer interface (BCI) experiment (Cho et al., 2017). This dataset is publicly available on the GigaScience Database (http://gigadb.org/dataset/100295), comprising 64-channel EEG recordings from 52 participants, sampled at 512 Hz (i.e., observations recorded approximately every  $\approx 1.95$  milliseconds). Each participant performed three oculomotor tasks—eye blinking, horizontal eye movement, and vertical eye movement—designed to support the development of motor imagery-based BCI research. Resting-state EEG recordings were also collected as control baselines.

Each oculomotor task spans a 5-second trial, yielding  $n=2560~(512\times5)$  observations

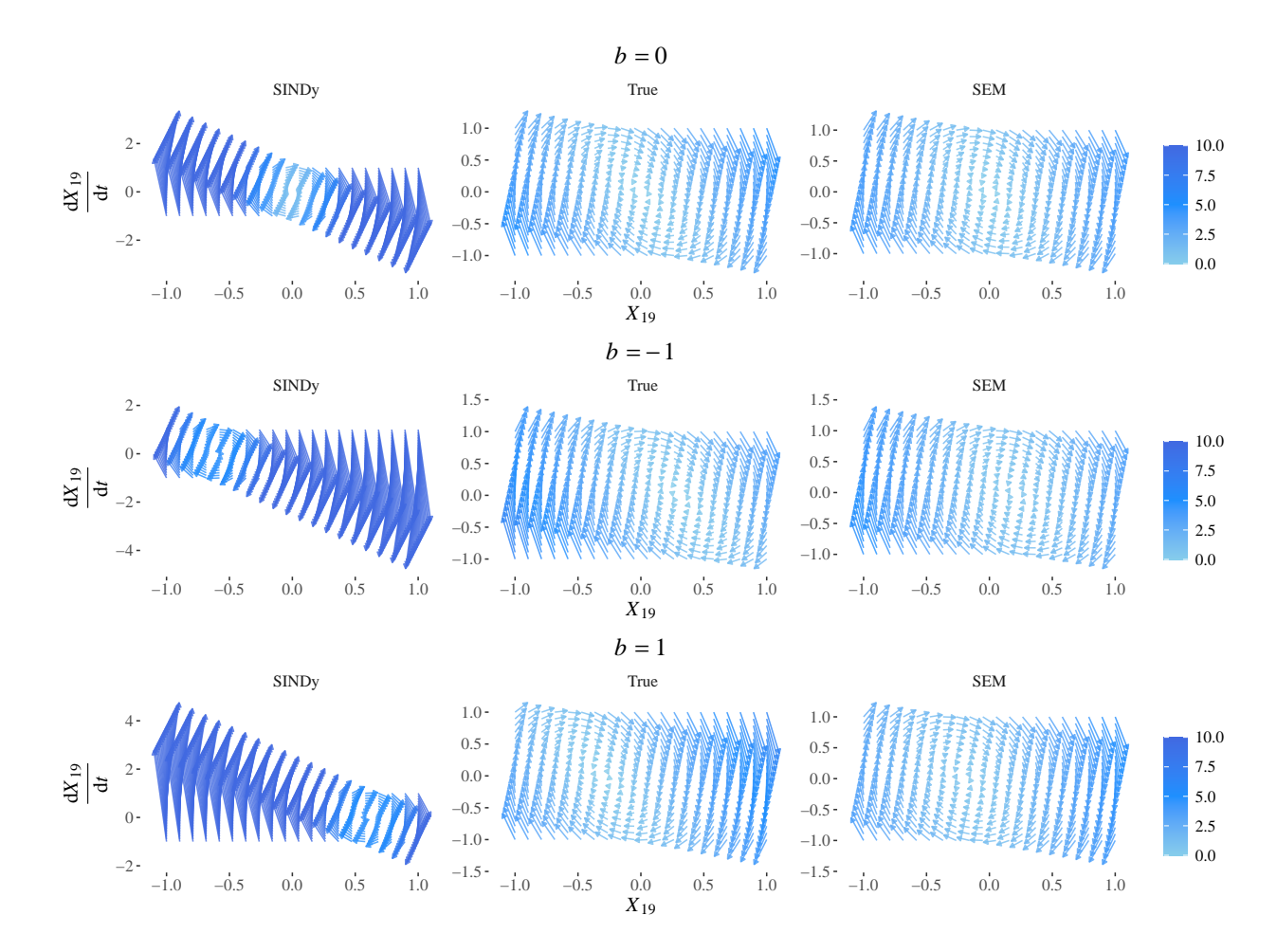


Figure 5: True and average estimated vector fields for  $X_{19}$  under three different values of b, based on 500 simulation runs with n=150 and  $\gamma=0.05$ . The color indicates the magnitude of the arrows.

per channel. In contrast, the resting-state recording lasts 60 seconds, yielding n=30720  $(512\times 60)$  time points per channel. For each task, the EEG data of the hth participant  $(h=1,\ldots,52)$  are denoted by  $Y_{ij}^{(h)}$ , where  $j\in\{1,\ldots,n\}$  indexes the observation time points and  $i\in\{1,\ldots,p\}$  indexes the EEG channels, with p=64 representing the total number of channels.

We apply the RKHS regression (7) on the noisy data  $\{Y_{ij}^{(h)}; i=1,\ldots,p,j=1,\ldots,n\}$  to recover smoothed latent trajectories  $\boldsymbol{X}^{(h)}=(\hat{X}_1^{(h)},\ldots,\hat{X}_p^{(h)})^{\top}$  for the h-th participant. The denoised curve is denoted as  $\hat{\boldsymbol{X}}^{(h)}$ . In Figure 6, we illustrate the denoised trajectories of some channels for the eye-blinking task, where we observe sustained oscillations in the EEG signals. Such oscillations may arise from the interplay between inertia and damping,

and their accurate description requires modeling acceleration—that is, using a second-order formulation. Due to this, we model the data using a second-order nonlinear differential equation:

$$\frac{\mathrm{d}^2 X_i^{(h)}(t)}{\mathrm{d}t^2} = -\omega_{i1} \frac{\mathrm{d} X_i^{(h)}}{\mathrm{d}t}(t) + \boldsymbol{H}^{\top} (\boldsymbol{X}^{(h)}(t)) \boldsymbol{\beta}_i, \quad i = 1, \dots, p,$$
(21)

where  $\boldsymbol{H}(\boldsymbol{X}^{(h)})$  contains candidate basis functions for modeling the dynamics. In our analysis, we construct  $\boldsymbol{H}(\boldsymbol{X}^{(h)})$  as in (17), using a polynomial basis of order P=2. Such forms of ODEs are widely adopted in the literature (Deco et al., 2008; Zhang et al., 2017; Brunton and Kutz, 2022) as they naturally accommodate the acceleration and damping effects often observed in neural data.

Prediction Performance For each participant and each oculomotor task, we apply SEM with LASSO penalty to estimate the underlying differential equations from  $\hat{X}^{(h)}$ . We also compare SEM to the benchmark method SINDy, which is widely used in brain dynamics and network discovery (Jansen and Rit, 1995; Friston et al., 2003; Zhang et al., 2020). To evaluate the performance of different methods, we partition each smoothed trajectory for the oculomotor task into a training interval  $(t \in [0,4))$  and a validation interval  $(t \in [4,5])$ . We then compute the predicted value  $\hat{X}_i^{(h),\text{pre}}(t_j)$ , obtained by solving the estimated differential system with initial condition  $\hat{X}^{(h)}(t_j - \Delta t)$ , where  $\Delta t$  is set as 0.015625 seconds. In Figure 6, we illustrate the predicted trajectories  $\hat{X}_i^{(h),\text{pre}}$  from SINDy and SEM, focusing on the eye-blinking task from three participants (indexed by h = 18, 25, 37) across three EEG channels (C3, CP5, and FT7). SEM predictions closely match the smoothed dynamics in the validation interval, whereas SINDy exhibits noticeable prediction bias.

Define the one-step-ahead relative prediction error (RPE) for the hth participant:

$$RPE_h := \frac{1}{p} \sqrt{\sum_{i=1}^{p} \frac{\sum_{j=1}^{T} \left( \hat{X}_i^{(h), \text{pre}}(t_j) - \hat{X}_i^{(h)}(t_j) \right)^2}{\sum_{j=1}^{T} \hat{X}_i^{(h)}(t_j)^2}},$$

where  $\{t_j\}_{j=1}^T$  are 512 equally spaced validation points in [4,5]. In Figure 7, we report the values of RPE<sub>h</sub> for all participants under the eye-blinking, horizontal eye movement, and vertical eye movement tasks. The results show that SEM consistently outperforms SINDy across these tasks. The unsatisfactory performance of SINDy may be attributed to errors arising from the estimation of high-order derivatives. In contrast, SEM circumvents the estimation of derivatives, resulting in more accurate data predictions.

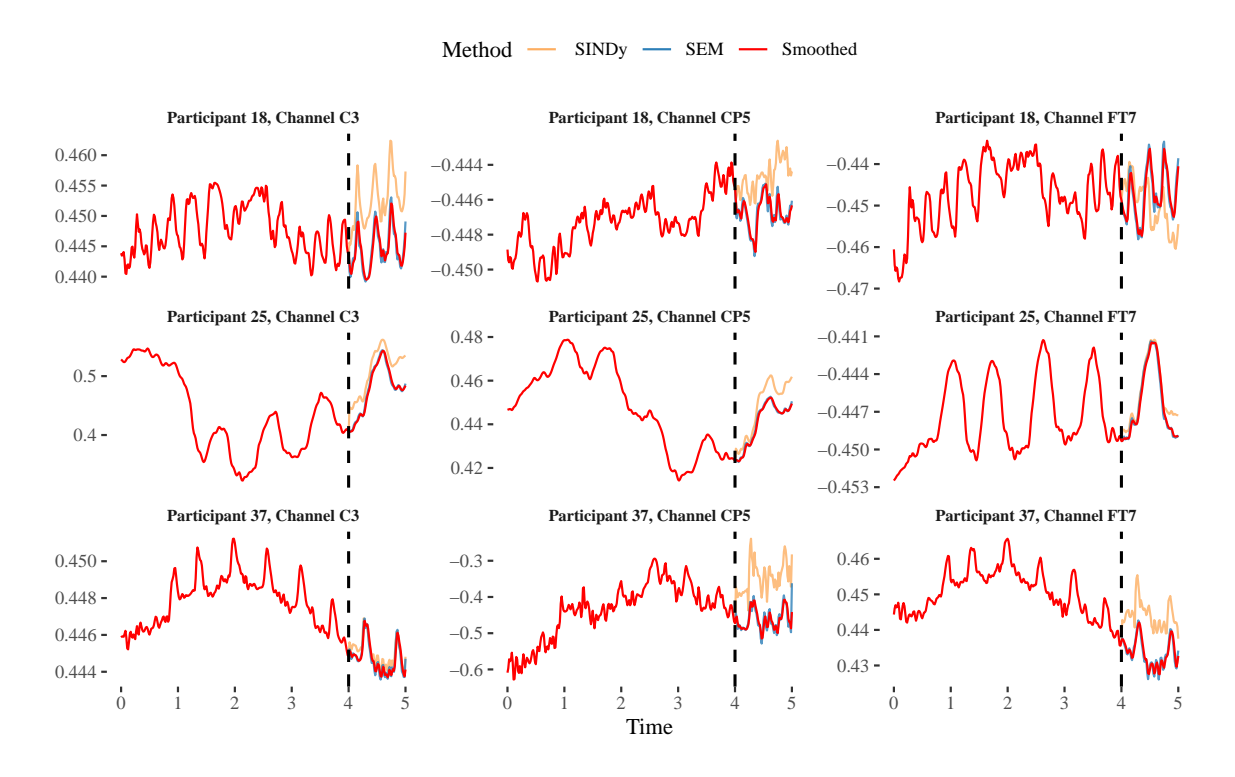


Figure 6: Smoothed and predicted dynamics of the eye-blinking task for channels C3, CP5, and FT7 from participants h = 18, 25, 37. Dashed vertical lines indicate the transition from the training interval (t < 4) to the validation interval  $(t \ge 4)$ .

**Brain Network Discovery** Based on the equations discovered by SEM, we construct directed brain networks for each participant and each oculomotor task. Let  $E = \{e_{i,j}\}_{i,j=1}^p$ 

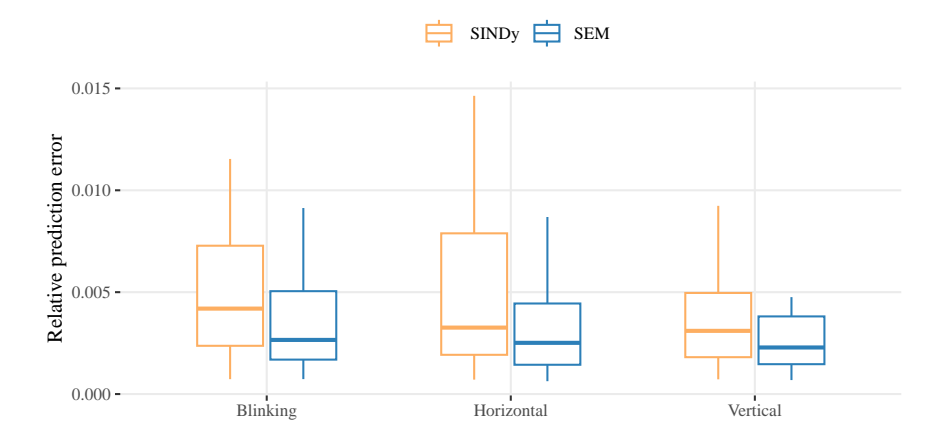


Figure 7: Boxplots of relative prediction errors (RPE) for 52 participants across three oculomotor tasks: eye blinking (blinking), horizontal eye movement (horizontal), andvertical eye movement (vertical). The RPE is evaluated on the held-out validation interval [4, 5].

denote the adjacency matrix derived from the dynamical model in (21), where  $e_{i,j} = 1$  if  $X_j$  contributes to the second-order derivative of  $X_i$  and  $e_{i,j} = 0$  otherwise. For each participant  $h \in \{1, \ldots, 52\}$ , we estimate an individual-specific adjacency matrix  $\hat{E}^{(h)} = \{\hat{e}_{i,j}^{(h)}\}_{i,j=1}^p$  from the discovered dynamics, resulting in a total of 52 networks for each task. To infer the population-level network, we treat  $\hat{E}^{(h)}$ ,  $h \in \{1, \ldots, 52\}$ , as repeated observations of E, and assume that the edge  $e_{i,j}$  is sampled from Bernoulli $(p_{i,j})$ . Under this, we test for the presence of each edge  $e_{i,j}$  by conducting a one-sided hypothesis test:

$$H_0: p_{i,j} \le 0.5 \quad \text{versus} \quad H_1: p_{i,j} > 0.5,$$
 (22)

at significance level  $\alpha = 0.05$ . We evaluate this test using a hypothesis test for each edge  $e_{i,j}$ , based on the collection of individual estimates  $\{\hat{E}^{(h)}\}_{h=1}^{52}$ .

Note that the above task is a multiple testing problem, we apply the Benjamini–Hochberg (BH) procedure (Benjamini and Hochberg, 1995) to ensure that the false discovery rate of tests is controlled below 5%. The resulting significant edges for the resting state and the three oculomotor tasks are shown in Figure 10 in Appendix B. We observe that the three

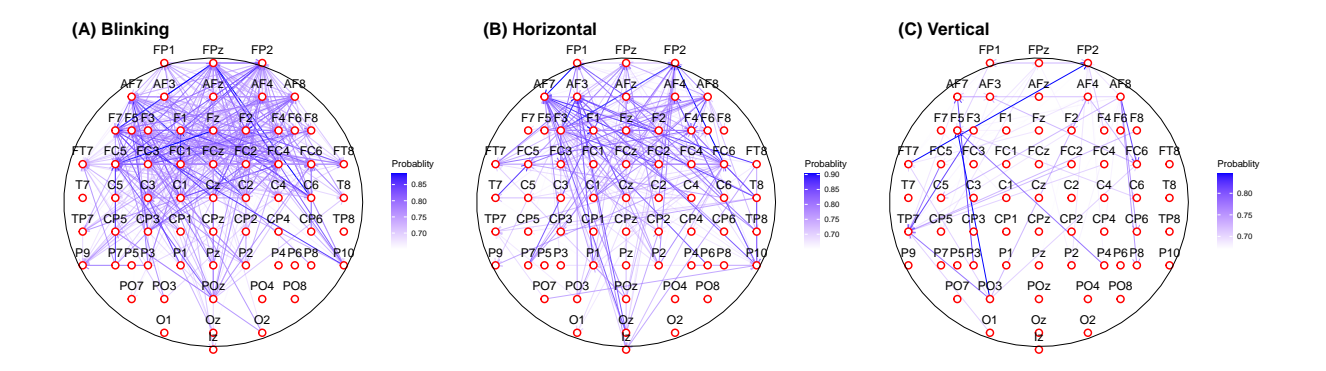


Figure 8: Directed brain networks for the eye-blinking, horizontal eye movement, and vertical eye movement tasks. Edge color represents the empirical probability of occurrence of each edge across participants.

oculomotor tasks exhibit distinct network patterns, while no significant directed edges are detected in the resting state.

To further investigate task-specific brain networks, we construct a second type of network that identifies edges more active during oculomotor tasks than during the resting state. Specifically, let  $E^0 = \{e^0_{i,j}\}_{i,j=1}^p$  and  $E^1 = \{e^1_{i,j}\}_{i,j=1}^p$  denote the adjacency matrices under the resting-state condition and a given oculomotor task, respectively. For each edge (i,j), we perform a one-sided Fisher's exact test to assess the null hypothesis:

$$H_0: \mathbb{P}(e_{i,j}^1 = 1) \le \mathbb{P}(e_{i,j}^0 = 1)$$
 versus  $H_1: \mathbb{P}(e_{i,j}^1 = 1) > \mathbb{P}(e_{i,j}^0 = 1)$ ,

at a significance level of  $\alpha = 0.05$ . We similarly apply the BH procedure to control the false discovery rate at 5%. Edges found to be significant in both the original test in (22) and the Fisher's exact test above are retained to construct a refined network. The resulting networks for the three oculomotor tasks are shown in Figure 8.

We compute several node-level metrics: out-degree, in-degree, betweenness centrality, and closeness centrality (Rubinov and Sporns, 2010)—to identify active brain regions in Figure 8. Specifically, out-degree and in-degree reflect a node's tendency to initiate or receive information, respectively. Betweenness centrality quantifies the extent to which a

node serves as a bridge along communication paths, while closeness centrality measures how efficiently a node can reach all other nodes in the network. These metrics for the three oculomotor tasks are provided in Appendix B.

In the eye-blinking task, we observe that significant brain connectivity is concentrated in the prefrontal region (see Figure 8 (A)). Within this region, channels FP2, F7, F5, and FPz exhibit high betweenness centrality (see Figure 11 (A) in Appendix B). In addition, FP2 and F5 also show high in-degree values (see Figure 11 (C) in Appendix B), with FP2 exhibiting a relatively high out-degree (see Figure 11 (D) in Appendix B). For the horizontal eye movement task, we similarly observe significant connectivity in the prefrontal region (see Figure 8 (B)). The prefrontal channels F3, AF4, AF3, and AF8 exhibit high betweenness centrality (see Figure 12 (A) in Appendix B), while AF7, FP2, and AF3 show high in-degree values (see Figure 12 (C) in Appendix B).

In the vertical eye movement task, we observe a posterior-to-anterior connectivity pattern (see Figure 8 (C)), characterized by a directed link from PO3 to F5. Channels FP2, FT7, and AF4 show high betweenness centrality (see Figure 13 (A) in Appendix B), with FT7 also exhibiting a high in-degree (see Figure 13 (C) in Appendix B).

Based on the above results, we identify prominent neural activity in the frontal cortical region, particularly involving channels such as FP2, F7, F5, FPz, AF3, and AF8—areas known to be associated with oculomotor control (Kato and Miyauchi, 2003; van Koningsbruggen et al., 2012). Among them, channel FP2 consistently exhibits high centrality across all three tasks, indicating its potential role as a central hub for oculomotor coordination. This channel is located over the right prefrontal cortex, which has been shown to be related to executive functions and voluntary saccadic regulation (Funahashi, 2014).

For the horizontal eye movements, we find that high-centrality nodes exhibit a bilaterally symmetric distribution (e.g., AF4, AF8  $\leftrightarrow$  AF3, AF7), suggesting that the task may involve interhemispheric coordination mechanisms. In contrast, vertical eye movements show

a distinct anterior—posterior connectivity pattern (e.g., PO3  $\rightarrow$  F5), with weaker bilateral connectivity compared to the horizontal task. As noted in the literature, vertical eye movements may rely more heavily on intrahemispheric signal transmission—such as the anterior—posterior pathways—during oculomotor control (Horn and Leigh, 2011; Leigh and Zee, 2015). Our findings support this phenomenon, revealing significant connectivity differences between horizontal and vertical eye movements.

### 6 Discussion

In this article, we propose a novel sparse equation matching (SEM) framework for equation discovery in general-order dynamical systems. Our approach unifies a broad class of existing methods through Green's function representations, enabling derivative-free estimation of both general-order differential operators and driving functions from dynamic data. The effectiveness of SEM is demonstrated through extensive simulations, showcasing the advantage of SEM over derivative-based methods in discovering general-order dynamics.

We further apply SEM to EEG data collected during multiple oculomotor tasks, uncovering meaningful and interpretable brain connectivity patterns based on the second-order signals of the data. In particular, we find that the prefrontal brain region is consistently active across all oculomotor tasks. Moreover, SEM identifies task-specific connectivity mechanisms: horizontal eye movements are associated with strong interhemispheric coordination, whereas vertical eye movements rely more on intrahemispheric pathways. These findings reveal significant differences in brain connectivity patterns across oculomotor tasks.

The SEM framework has some limitations. First, our method focuses on sparse equation matching using a predefined set of candidate basis functions. Alternative approaches—such as Gaussian processes (Heinonen et al., 2018), RKHS (Bobade et al., 2019; Dai and Li, 2022), symbolic regression (Qian et al., 2022), and neural networks (Chen et al., 2018, 2025)—could

be integrated into our framework to explore broader structural forms of equations. Second, SEM relies on a pre-estimation step for trajectory recovery, making it a two-step procedure for differential equation learning. This approach is well-suited for densely observed data like the EEG data in our analysis, where the trajectory pre-estimates can be reliably obtained. However, in settings with sparse observations, the pre-estimation step may introduce inaccuracies to the subsequent equation discovery. Methods that jointly estimate the trajectory and the underlying differential equation, such as Ramsay et al. (2007); Raissi et al. (2019); Yang et al. (2021), could offer a more robust alternative in such scenarios. Extending SEM to incorporate joint estimation is an important direction for future research.

### Acknowledgements

Xueqin Wang's research is supported in part by NSFC-12231017 and NSFC-72171216.

# References

Balla, J., Huang, S., Dugan, O., Dangovski, R. and Soljačić, M. (2025), 'Ai-assisted discovery of quantitative and formal models in social science', *Humanities and Social Sciences Communications* **12**(1), 1–12.

Benjamini, Y. and Hochberg, Y. (1995), 'Controlling the false discovery rate: a practical and powerful approach to multiple testing', *Journal of the Royal statistical society: series B (Methodological)* **57**(1), 289–300.

Bobade, P., Majumdar, S., Pereira, S., Kurdila, A. J. and Ferris, J. B. (2019), 'Adaptive estimation for nonlinear systems using reproducing kernel hilbert spaces', *Advances in Computational Mathematics* **45**, 869–896.

- Brückner, D. B. and Broedersz, C. P. (2024), 'Learning dynamical models of single and collective cell migration: a review', *Reports on Progress in Physics* 87(5), 056601.
- Brunton, S. L. and Kutz, J. N. (2022), Data-driven science and engineering: Machine learning, dynamical systems, and control, Cambridge University Press, Cambridge, UK.
- Brunton, S. L., Proctor, J. L. and Kutz, J. N. (2016), 'Discovering governing equations from data by sparse identification of nonlinear dynamical systems', *Proceedings of the national academy of sciences* **113**(15), 3932–3937.
- Carrillo, J. A., Choi, Y.-P. and Perez, S. P. (2017), 'A review on attractive–repulsive hydrodynamics for consensus in collective behavior', *Active Particles, Volume 1: Advances in Theory, Models, and Applications* pp. 259–298.
- Champion, K., Lusch, B., Kutz, J. N. and Brunton, S. L. (2019), 'Data-driven discovery of coordinates and governing equations', *Proceedings of the National Academy of Sciences* **116**(45), 22445–22451.
- Chen, R. T., Rubanova, Y., Bettencourt, J. and Duvenaud, D. K. (2018), 'Neural ordinary differential equations', Advances in neural information processing systems 31.
- Chen, S., Shojaie, A. and Witten, D. M. (2017), 'Network reconstruction from high-dimensional ordinary differential equations', *Journal of the American Statistical Association* **112**(520), 1697–1707.
- Chen, Z., Yan, S. and Yao, F. (2025), 'Deep semiparametric partial differential equation models', arXiv preprint arXiv:2506.22779.
- Cho, H., Ahn, M., Ahn, S., Kwon, M. and Jun, S. C. (2017), 'Eeg datasets for motor imagery brain-computer interface', *GigaScience* **6**(7), gix034.

- Cox, D. D. (1983), 'Asymptotics for m-type smoothing splines', *The Annals of Statistics* pp. 530–551.
- Dai, X. and Li, L. (2022), 'Kernel ordinary differential equations', Journal of the American Statistical Association 117(540), 1711–1725.
- Dattner, I. and Klaassen, C. A. (2015), 'Optimal rate of direct estimators in systems of ordinary differential equations linear in functions of the parameters', *Electronic Journal of Statistics*.
- Deco, G., Jirsa, V. K., Robinson, P. A., Breakspear, M. and Friston, K. (2008), 'The dynamic brain: from spiking neurons to neural masses and cortical fields', *PLoS computational biology* 4(8), e1000092.
- Duffy, D. G. (2015), *Green's functions with applications*, Chapman and Hall/CRC, New York.
- Egan, K., Li, W. and Carvalho, R. (2024), 'Automatically discovering ordinary differential equations from data with sparse regression', *Communications Physics* **7**(1), 20.
- Fasel, U., Kutz, J. N., Brunton, B. W. and Brunton, S. L. (2022), 'Ensemble-sindy: Robust sparse model discovery in the low-data, high-noise limit, with active learning and control', *Proceedings of the Royal Society A* 478(2260), 20210904.
- Friston, K. J. (2011), 'Functional and effective connectivity: a review', *Brain connectivity* 1(1), 13–36.
- Friston, K. J., Harrison, L. and Penny, W. (2003), 'Dynamic causal modelling', *Neuroimage* 19(4), 1273–1302.
- Funahashi, S. (2014), 'Saccade-related activity in the prefrontal cortex: its role in eye movement control and cognitive functions', Frontiers in integrative neuroscience 8, 54.

- Gu, C. and Gu, C. (2013), Smoothing spline ANOVA models, Vol. 297, Springer, New York.
- Hairer, E., Lubich, C. and Wanner, G. (2006), Geometric Numerical Integration: Structure-Preserving Algorithms for Ordinary Differential Equations, Springer-Verlag, Berlin.
- Hastie, T., Tibshirani, R. and Friedman, J. (2017), The elements of statistical learning: data mining, inference, and prediction, Springer, New York.
- Heinonen, M., Yildiz, C., Mannerström, H., Intosalmi, J. and Lähdesmäki, H. (2018), Learning unknown ode models with gaussian processes, *in* 'International conference on machine learning', PMLR, pp. 1959–1968.
- Horn, A. K. and Leigh, R. J. (2011), 'The anatomy and physiology of the ocular motor system', *Handbook of clinical neurology* **102**, 21–69.
- Hsing, T. and Eubank, R. (2015), Theoretical foundations of functional data analysis, with an introduction to linear operators, Vol. 997, John Wiley & Sons, Chichester, UK.
- Jansen, B. H. and Rit, V. G. (1995), 'Electroencephalogram and visual evoked potential generation in a mathematical model of coupled cortical columns', *Biological cybernetics* **73**(4), 357–366.
- Kaiser, E., Kutz, J. N. and Brunton, S. L. (2018), 'Sparse identification of nonlinear dynamics for model predictive control in the low-data limit', Proceedings of the Royal Society A 474(2219), 20180335.
- Kato, M. and Miyauchi, S. (2003), 'Functional mri of brain activation evoked by intentional eye blinking', *Neuroimage* **18**(3), 749–759.
- Kiebel, S. J., Garrido, M. I., Moran, R., Chen, C.-C. and Friston, K. J. (2009), 'Dynamic causal modeling for eeg and meg', *Human Brain Mapping* **30**(6), 1866–1876.

- Leigh, R. J. and Zee, D. S. (2015), *The neurology of eye movements*, Oxford university press, Oxford, UK.
- Lorenz, E. N. (2017), Deterministic nonperiodic flow 1, in 'Universality in Chaos, 2nd edition', Routledge, New York, pp. 367–378.
- Lu, F., Zhong, M., Tang, S. and Maggioni, M. (2019), 'Nonparametric inference of interaction laws in systems of agents from trajectory data', *Proceedings of the National Academy of Sciences* **116**(29), 14424–14433.
- Lu, L., Jin, P., Pang, G., Zhang, Z. and Karniadakis, G. E. (2021), 'Learning nonlinear operators via deeponet based on the universal approximation theorem of operators', *Nature machine intelligence* **3**(3), 218–229.
- Meirovitch, L. (2010), Fundamentals of Vibrations, Waveland Press, Long Grove, IL.
- Messenger, D. A. and Bortz, D. M. (2021), 'Weak sindy for partial differential equations',

  Journal of Computational Physics 443, 110525.
- Niedermeyer, E. and da Silva, F. L. (2005), Electroencephalography: basic principles, clinical applications, and related fields, Lippincott Williams & Wilkins, Philadelphia, PA.
- Owens, K. and Kutz, J. N. (2023), 'Data-driven discovery of governing equations for coarse-grained heterogeneous network dynamics', SIAM Journal on Applied Dynamical Systems **22**(3), 2601–2623.
- Qian, Z., Kacprzyk, K. and van der Schaar, M. (2022), D-code: Discovering closed-form odes from observed trajectories, *in* 'International Conference on Learning Representations'.
- Raissi, M., Perdikaris, P. and Karniadakis, G. E. (2019), 'Physics-informed neural networks:

  A deep learning framework for solving forward and inverse problems involving nonlinear partial differential equations', *Journal of Computational physics* 378, 686–707.

- Ramsay, J. and Hooker, G. (2017), 'Dynamic data analysis', Springer New York, New York, NY. doi 10, 978–1.
- Ramsay, J. O., Hooker, G., Campbell, D. and Cao, J. (2007), 'Parameter estimation for differential equations: a generalized smoothing approach', *Journal of the Royal Statistical Society Series B: Statistical Methodology* **69**(5), 741–796.
- Rubinov, M. and Sporns, O. (2010), 'Complex network measures of brain connectivity: uses and interpretations', *Neuroimage* **52**(3), 1059–1069.
- Schaeffer, H. and McCalla, S. G. (2017), 'Sparse model selection via integral terms', *Physical Review E* **96**(2), 023302.
- Shao, L. and Yao, F. (2025), 'Ordinary differential equation models for a collection of discretized functions', Journal of the Royal Statistical Society Series B: Statistical Methodology p. qkaf036.
- Shumway, R. H., Stoffer, D. S. and Stoffer, D. S. (2000), Time series analysis and its applications, Vol. 3, Springer, New York.
- Sporns, O. (2016), Networks of the Brain, MIT press, Cambridge, MA.
- Stein, K., Timmermann, A., Schneider, N., Jin, F.-F. and Stuecker, M. F. (2014), 'Enso seasonal synchronization theory', *Journal of Climate* **27**(14), 5285–5310.
- Tan, J., Ge, Y., Martinez, L., Sun, J., Li, C., Westbrook, A., Chen, E., Pan, J., Li, Y., Cheng, W. et al. (2022), 'Transmission roles of symptomatic and asymptomatic covid-19 cases: a modelling study', *Epidemiology & Infection* **150**, e171.
- Tan, J., Shen, Y., Ge, Y., Martinez, L. and Huang, H. (2023), 'Age-related model for estimating the symptomatic and asymptomatic transmissibility of covid-19 patients', *Biometrics* **79**(3), 2525–2536.

- Tan, J., Shi, P. and Zhang, A. R. (2024), 'Functional singular value decomposition', arXiv preprint arXiv:2410.03619.
- Tan, J., Zhang, G., Wang, X., Huang, H. and Yao, F. (2024), 'Green's matching: an efficient approach to parameter estimation in complex dynamic systems', *Journal of the Royal Statistical Society Series B: Statistical Methodology* p. qkae031.
- Thompson, J. M. T. and Stewart, H. B. (2002), *Nonlinear dynamics and chaos*, John Wiley & Sons, New York.
- Tian, T., Tan, J., Luo, W., Jiang, Y., Chen, M., Yang, S., Wen, C., Pan, W. and Wang, X. (2021), 'The effects of stringent and mild interventions for coronavirus pandemic', Journal of the American Statistical Association 116(534), 481–491.
- Valdes-Sosa, P. A., Roebroeck, A., Daunizeau, J. and Friston, K. (2011), 'Effective connectivity: influence, causality and biophysical modeling', *Neuroimage* **58**(2), 339–361.
- van Koningsbruggen, M. G., Peelen, M. V., Davies, E. and Rafal, R. D. (2012), 'Neural control of voluntary eye closure: a case study and an fmri investigation of blinking and winking', *Behavioural neurology* **25**(2), 103–109.
- Wahba, G. (1990), Spline models for observational data, SIAM, Philadelphia.
- Wu, H., Lu, T., Xue, H. and Liang, H. (2014), 'Sparse additive ordinary differential equations for dynamic gene regulatory network modeling', Journal of the American Statistical Association 109(506), 700–716.
- Yang, S., Wong, S. W. and Kou, S. (2021), 'Inference of dynamic systems from noisy and sparse data via manifold-constrained gaussian processes', *Proceedings of the National Academy of Sciences* 118(15), e2020397118.

- Yuan, M. and Lin, Y. (2006), 'Model selection and estimation in regression with grouped variables', Journal of the Royal Statistical Society Series B: Statistical Methodology 68(1), 49–67.
- Zhang, T., Sun, Y., Li, H., Yan, G., Tanabe, S., Miao, R., Wang, Y., Caffo, B. S. and Quigg, M. S. (2020), 'Bayesian inference of a directional brain network model for intracranial eeg data', Computational Statistics & Data Analysis 144, 106847.
- Zhang, T., Yin, Q., Caffo, B., Sun, Y. and Boatman-Reich, D. (2017), 'Bayesian inference of high-dimensional, cluster-structured ordinary differential equation models with applications to brain connectivity studies', *The Annals of Applied Statistcs*.
- Zhu, J., Wen, C., Zhu, J., Zhang, H. and Wang, X. (2020), 'A polynomial algorithm for best-subset selection problem', *Proceedings of the National Academy of Sciences* **117**(52), 33117–33123.
- Zou, H. and Hastie, T. (2005), 'Regularization and variable selection via the elastic net',

  Journal of the Royal Statistical Society Series B: Statistical Methodology 67(2), 301–320.

## A Technical Proof

### A.1 Proof of Theorem 1

*Proof.* We divide the proof into two parts based on the value of k.

When k = 0, by definition,  $G^0(t, s) = \delta(t - s)$ , and the kernel term  $g_0(t) \equiv 0$ . Then the integral equation (13) reduces to:

$$\frac{\mathrm{d}^{K} X_{i}}{\mathrm{d}t^{K}}(t) + \sum_{l=1}^{K-1} \omega_{il} \frac{\mathrm{d}^{l} X_{i}}{\mathrm{d}t^{l}}(t) = f_{i}(\boldsymbol{X}(t), t),$$

which is exactly the original differential equation (3).

Then, let  $k \geq 1$  be fixed. Applying the Green's function  $G^k$  to both sides of (3), we obtain:

$$\int_{0}^{C} G^{k}(t,s) \left( \frac{\mathrm{d}^{K} X_{i}}{\mathrm{d}t^{K}}(s) + \sum_{l=1}^{K-1} \omega_{il} \frac{\mathrm{d}^{l} X_{i}}{\mathrm{d}t^{l}}(s) \right) \mathrm{d}s$$

$$= \int_{0}^{C} G^{k}(t,s) f_{i}(\boldsymbol{X}(s),s) \, \mathrm{d}s.$$
(23)

By the definition of  $G^k(t, s)$  in (12), we repeatedly apply integration by parts and obtain, for  $l \ge k$ ,

$$\begin{split} \int_0^C G^k(t,s) \frac{\mathrm{d}^l X_i}{\mathrm{d}s^l}(s) \, \mathrm{d}s &= \int_0^C \frac{(t-s)^{k-1}}{(k-1)!} \, \mathbb{I}(s \le t) \frac{\mathrm{d}^l X_i}{\mathrm{d}t^l}(s) \mathrm{d}s \\ &= -\frac{t^{k-1}}{(k-1)!} \frac{\mathrm{d}^{l-1} X_i}{\mathrm{d}t^{l-1}}(0) + \int_0^C G^{k-1}(t,s) \frac{\mathrm{d}^{l-1} X_i}{\mathrm{d}t^{l-1}}(s) \mathrm{d}s \\ &= \dots = -\sum_{m=1}^k \frac{\mathrm{d}^{l-m} X_i}{\mathrm{d}t^{l-m}}(0) \frac{t^{k-m}}{(k-m)!} + \frac{\mathrm{d}^{l-k} X_i}{\mathrm{d}t^{l-k}}(t), \\ &= \frac{\mathrm{d}^{l-k} X_i}{\mathrm{d}t^{l-k}}(t) + g_{ik}^{(l)}(t), \end{split}$$

where the the correction term  $g_{ik}^{(l)}(t) \in \operatorname{Ker}\left(\frac{\mathrm{d}^k}{\mathrm{d}t^k}\right)$ .

For l < k, we have:

$$\int_0^C G^k(t,s) \frac{\mathrm{d}^l X_i}{\mathrm{d}s^l}(s) \, \mathrm{d}s = \int_0^C G^{k-l}(t,s) X_i(s) \, \mathrm{d}s + g_{ik}^{(l)}(t),$$

where  $g_{ik}^{(l)}(t) \in \text{Ker}\left(\frac{d^k}{dt^k}\right)$ . Applying this to each term in (23), we obtain:

• For the main term:

$$\int_{0}^{C} G^{k}(t,s) \frac{\mathrm{d}^{K} X_{i}}{\mathrm{d}s^{K}}(s) \, \mathrm{d}s = \frac{\mathrm{d}^{K-k} X_{i}}{\mathrm{d}t^{K-k}}(t) + g_{ik}^{(K)}(t).$$

• For  $l \in \{k+1, \dots, K-1\}$ :

$$\int_0^C G^k(t,s) \frac{d^l X_i}{ds^l}(s) ds = \frac{d^{l-k} X_i}{dt^{l-k}}(t) + g_{ik}^{(l)}(t).$$

• For  $l \in \{1, ..., \min(k, K - 1)\}$ :

$$\int_0^C G^k(t,s) \frac{d^l X_i}{ds^l}(s) ds = \int_0^C G^{k-l}(t,s) X_i(s) ds + g_{ik}^{(l)}(t).$$

Substituting all terms into equation (23), we we arrive at:

$$\frac{\mathrm{d}^{K-k}X_{i}}{\mathrm{d}t^{K-k}}(t) + \sum_{l=k+1}^{K-1} \omega_{il} \frac{\mathrm{d}^{l-k}X_{i}}{\mathrm{d}t^{l-k}}(t) + \sum_{l=1}^{\min(k,K-1)} \omega_{il} \int_{0}^{C} G^{k-l}(t,s)X_{i}(s) \,\mathrm{d}s$$

$$= g_{ik}(t) + \int_{0}^{C} G^{k}(t,s)f_{i}(\boldsymbol{X}(s),s) \,\mathrm{d}s,$$

where  $g_{ik}(t) := g_{ik}^{(K)}(t) + \sum_{l=1}^{K-1} \omega_{il} g_{ik}^{(l)}(t) \in \operatorname{Ker}\left(\frac{\mathrm{d}^k}{\mathrm{d}t^k}\right)$ .

Specially, when k=0,  $\min(k,K-1)=0$ , so the third summation vanishes. When  $k\geq K-1$ , the second summation over  $l=k+1,\ldots,K-1$  becomes empty and thus is omitted. When  $k\geq K$ , the first term  $\frac{\mathrm{d}^{K-k}X_i}{\mathrm{d}t^{K-k}}(t)$  is ill-defined, so we it by its integral

counterpart:  $\int_0^C G^{k-K}(t,s)X_i(s) ds$ . This completes the proof.

### A.2 Proof of Theorem 2

*Proof.* For

$$\widetilde{G}^k(t,s) = G^k(t,s) + \boldsymbol{\Phi}_k^{\top}(t) \, \boldsymbol{v}_k(s), \ k = 1, 2, \dots, K,$$

we have the following identities:

$$\int_0^C \tilde{G}^k(t,s) X_i(s) \mathrm{d}s = \int_0^C G^k(t,s) X_i(s) \mathrm{d}s + \boldsymbol{\Phi}_k^\top(t) \int_0^C \boldsymbol{v}_k(s) X_i(s) \mathrm{d}s, \ 1 \le k \le K - 1,$$
$$\int_0^C \tilde{G}^K(t,s) \boldsymbol{H}^\top(\boldsymbol{X}(s)) \mathrm{d}s = \int_0^C G^K(t,s) \boldsymbol{H}^\top(\boldsymbol{X}(s)) \mathrm{d}s + \boldsymbol{\Phi}_K^\top(t) \int_0^C \boldsymbol{v}_K(s) \boldsymbol{H}^\top(\boldsymbol{X}(s)) \mathrm{d}s.$$

Substituting into the definition of  $\tilde{\Theta}_i$  in Theorem 2, we obtain:

$$\tilde{\boldsymbol{\Theta}}_{i}(\boldsymbol{X}(t)) = \boldsymbol{\Theta}_{i}(\boldsymbol{X}(t)) + \left(\boldsymbol{\Phi}_{K-1}^{\top}(t) \int_{0}^{C} \boldsymbol{v}_{K-1}(s) X_{i}(s) \mathrm{d}s, \ldots, \right.$$
$$\boldsymbol{\Phi}_{1}^{\top}(t) \int_{0}^{C} \boldsymbol{v}_{1}(s) X_{i}(s) \mathrm{d}s, \boldsymbol{\Phi}_{K}^{\top}(t) \int_{0}^{C} \boldsymbol{v}_{K}(s) \boldsymbol{H}^{\top}(\boldsymbol{X}(s)) \mathrm{d}s \right).$$

Let  $\boldsymbol{\theta}_i = (-\omega_{i1}, \dots, -\omega_{i(K-1)}, \boldsymbol{\beta}_i^{\mathsf{T}})^{\mathsf{T}}$ , and  $\boldsymbol{\alpha}_i = (\alpha_1, \dots, \alpha_K)$ . Consider a transformed coefficient vector  $\tilde{\boldsymbol{\alpha}}_i = (\tilde{\alpha}_{i1}, \dots, \tilde{\alpha}_{iK})$  defined by

$$\tilde{\alpha}_{ik} = \alpha_{ik} + \sum_{l=k}^{K-1} \omega_{il} \int_0^C \psi_{lk}(s) X_i(s) ds - \int_0^C \psi_{Kk}(s) \boldsymbol{H}^\top (\boldsymbol{X}(s)) \boldsymbol{\beta}_i ds, \quad k = 1, \dots, K, \quad (24)$$

where the first summation term  $\sum_{l=k}^{K-1} \omega_{il} \int_0^C \psi_{lk}(s) X_i(s) ds$  is omitted when k=K.

With this transformation, we have

$$\tilde{\mathcal{F}}_{\boldsymbol{\theta}_i,\tilde{\boldsymbol{\alpha}}_i}^i(\boldsymbol{X},t) = \mathcal{F}_{\boldsymbol{\theta}_i,\boldsymbol{\alpha}_i}^i(\boldsymbol{X},t),$$

and consequently,

$$ilde{\mathcal{L}}_i(oldsymbol{ heta}_i, ilde{oldsymbol{lpha}}_i \mid oldsymbol{X}) = \mathcal{L}_i(oldsymbol{ heta}_i, oldsymbol{lpha}_i \mid oldsymbol{X})$$

for any fixed  $\theta_i$  if  $\alpha_i$  and  $\tilde{\alpha}_i$  satisfy (24).

Define the optimal values

$$M_1 := \min_{\boldsymbol{\theta}_i, \boldsymbol{\alpha}_i} \mathcal{L}_i(\boldsymbol{\theta}_i, \boldsymbol{\alpha}_i \mid \boldsymbol{X}), \quad M_2 := \min_{\boldsymbol{\theta}_i, \boldsymbol{\alpha}_i} \tilde{\mathcal{L}}_i(\boldsymbol{\theta}_i, \boldsymbol{\alpha}_i \mid \boldsymbol{X})$$

We now prove  $M_1 = M_2$ .

For any  $\epsilon > 0$ , there exists  $(\boldsymbol{\theta}_i^{\epsilon}, \boldsymbol{\alpha}_i^{\epsilon})$  such that

$$\mathcal{L}_i(\boldsymbol{\theta}_i^{\epsilon}, \boldsymbol{\alpha}_i^{\epsilon} \mid \boldsymbol{X}) < M_1 + \epsilon,$$

Define  $\tilde{\boldsymbol{\alpha}}_i$  using (24) with  $\boldsymbol{\alpha}_i = \boldsymbol{\alpha}_i^{\epsilon}$  and  $\boldsymbol{\theta}_i = \boldsymbol{\theta}_i^{\epsilon}$ . Then

$$M_2 \leq \tilde{\mathcal{L}}_i(\boldsymbol{\theta}_i^{\epsilon}, \tilde{\boldsymbol{\alpha}}_i \mid \boldsymbol{X}) = \mathcal{L}_i(\boldsymbol{\theta}_i^{\epsilon}, \boldsymbol{\alpha}_i^{\epsilon} \mid \boldsymbol{X}) < M_1 + \epsilon.$$

Letting  $\epsilon \to 0$  yields  $M_2 \le M_1$ . Similarly, using the inverse transformation in equation (25), one can show  $M_1 \le M_2$ . Therefore, we conclude that  $M_1 = M_2$ .

Now, if  $(\hat{\boldsymbol{\theta}}_i, \hat{\boldsymbol{\alpha}}_i)$  minimizes  $\mathcal{L}_i(\boldsymbol{\theta}_i, \boldsymbol{\alpha}_i \mid \boldsymbol{X})$ , define  $\tilde{\boldsymbol{\alpha}}_i$  using (24) with  $\boldsymbol{\alpha}_i = \hat{\boldsymbol{\alpha}}_i, \boldsymbol{\theta}_i = \hat{\boldsymbol{\theta}}_i$ . Then

$$\tilde{\mathcal{L}}_i(\hat{\boldsymbol{\theta}}_i, \tilde{\boldsymbol{\alpha}}_i \mid \boldsymbol{X}) = M_1 = M_2,$$

so  $(\hat{\boldsymbol{\theta}}_i, \tilde{\boldsymbol{\alpha}}_i)$  minimizes  $\tilde{\mathcal{L}}_i(\boldsymbol{\theta}_i, \boldsymbol{\alpha}_i \mid \boldsymbol{X})$ .

Conversely, if  $(\tilde{\boldsymbol{\theta}}_i, \tilde{\boldsymbol{\alpha}}_i)$  minimizes  $\tilde{\mathcal{L}}_i(\boldsymbol{\theta}_i, \boldsymbol{\alpha}_i \mid \boldsymbol{X})$ , let  $\tilde{\boldsymbol{\theta}}_i = (-\tilde{\omega}_{i1}, \dots, -\tilde{\omega}_{i(K-1)}, \tilde{\boldsymbol{\beta}}_i^{\top})^{\top}$  and

define  $\hat{\boldsymbol{\alpha}}_i = (\hat{\alpha}_{i1}, \dots, \hat{\alpha}_{iK})$  via the inverse transformation:

$$\hat{\alpha}_{ik} = \tilde{\alpha}_{ik} - \sum_{l=k}^{K-1} \tilde{\omega}_{il} \int_{0}^{C} \psi_{lk}(s) X_{i}(s) ds +$$

$$\int_{0}^{C} \psi_{Kk}(s) \boldsymbol{H}^{\top}(\boldsymbol{X}(s)) \tilde{\boldsymbol{\beta}}_{i} ds, \quad k = 1, \dots, K.$$
(25)

Then  $(\tilde{\boldsymbol{\theta}}_i, \hat{\boldsymbol{\alpha}}_i)$  minimizes  $\mathcal{L}_i(\boldsymbol{\theta}_i, \boldsymbol{\alpha}_i \mid \boldsymbol{X})$ .

By definition, there exists an identity map id and the bijection  $\mathcal{M}$  constructed via equation (25) such that

$$id(\tilde{\Theta}) = \hat{\Theta}, \text{ and } \mathcal{M}(\tilde{\mathcal{A}}) = \hat{\mathcal{A}}.$$

# **B** Supporting Results

### B.1 An Illustration for Dynamic Directional Models

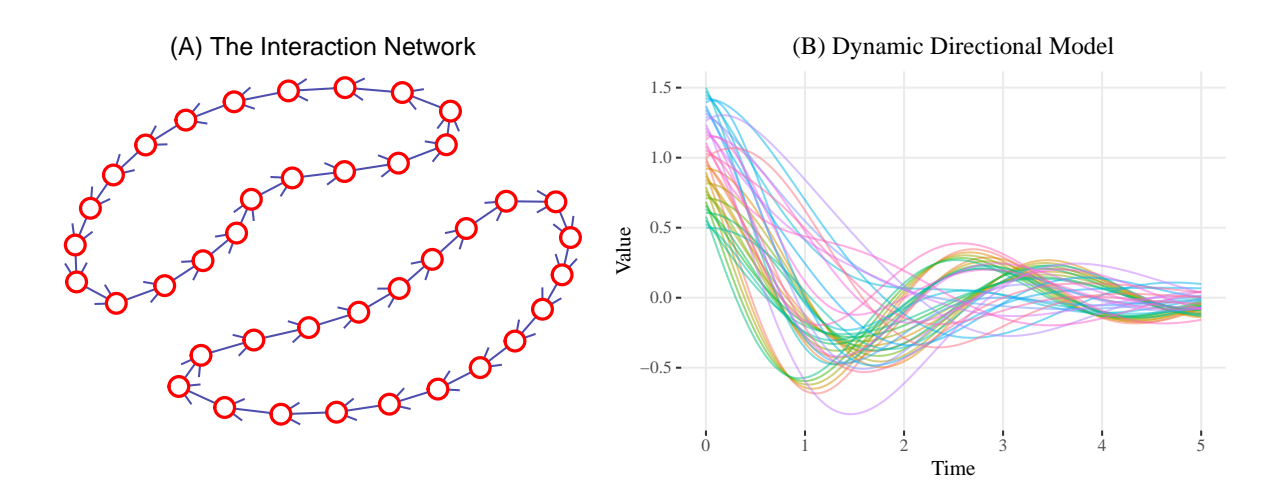


Figure 9: (A) The directed interaction network; Each node represents a neural mass unit whose dynamics are governed by local excitation, inter-node directional coupling, and proportional damping that stabilizes oscillatory amplitudes. The direction between two nodes indicates that the trajectory of one node is affected by that of the other according to the dynamic directional model. (B) The trajectories generated from the dynamic directional model.

## **B.2** Directed Brain Networks and Centrality Measures

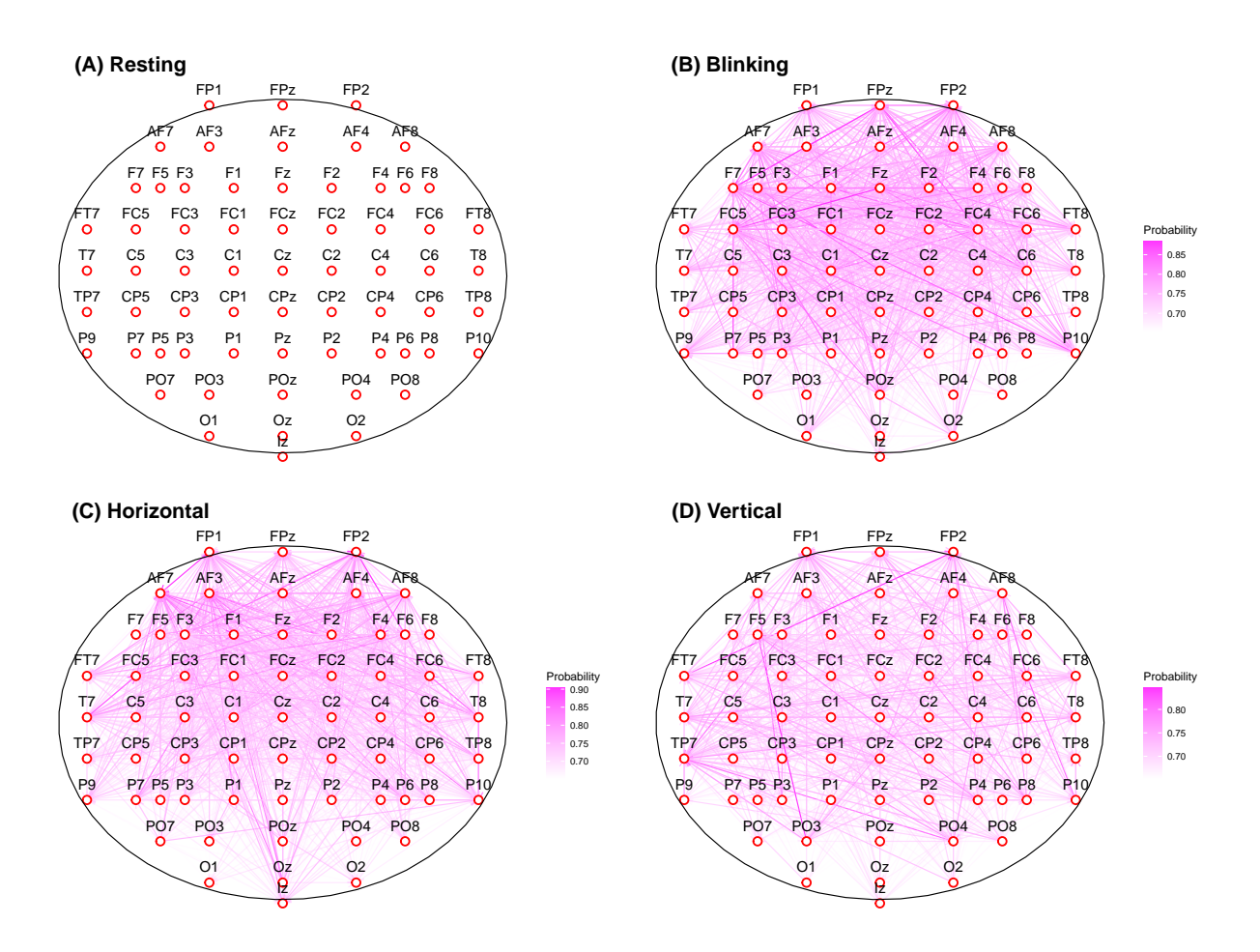


Figure 10: Directed brain networks for different tasks: (A) resting state, (B) eye-blinking, (C) horizontal eye movement, (D) vertical eye movement. Edge color indicates the empirical probability of each edge occurring across participants.

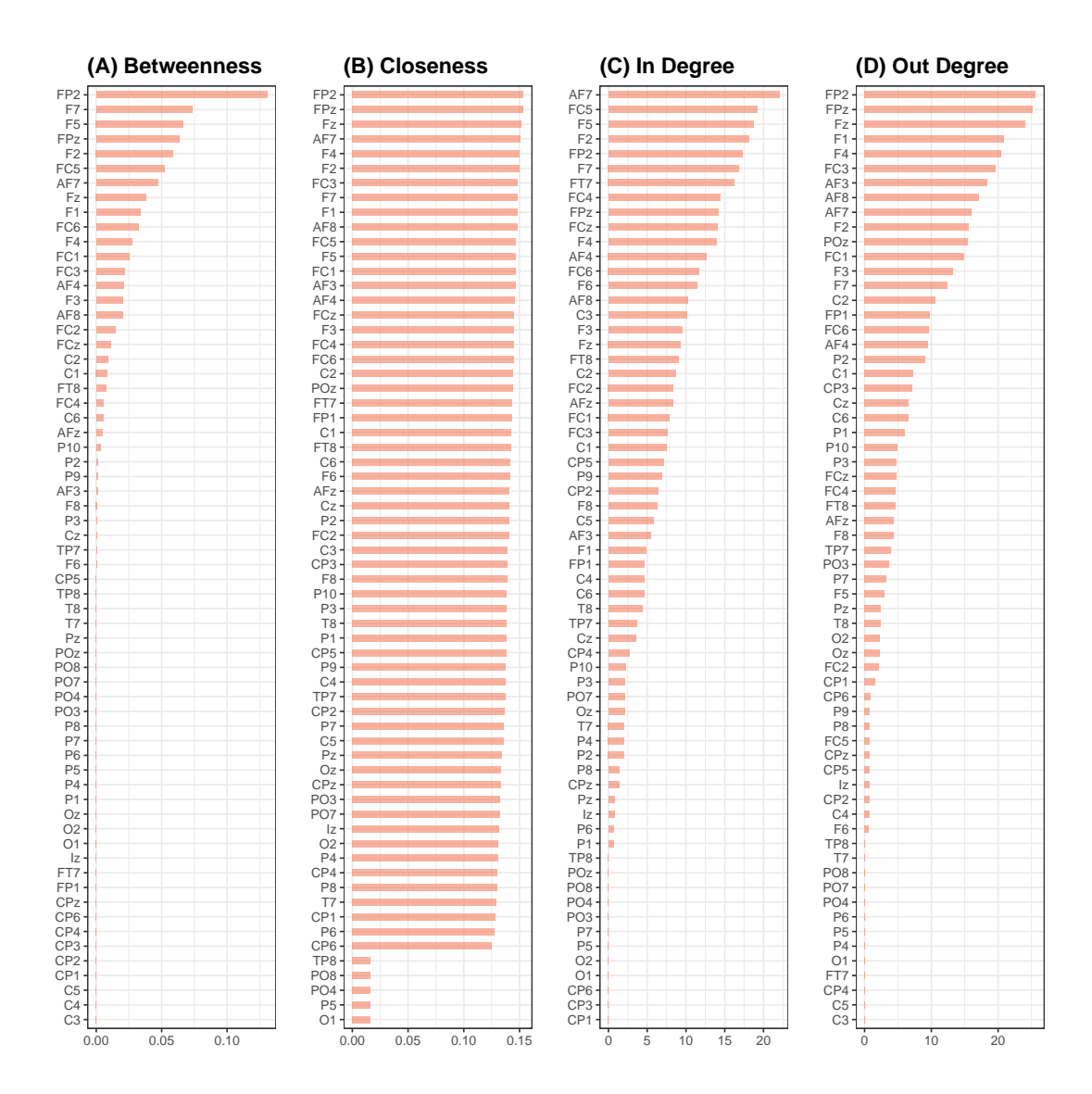


Figure 11: A comparison of centrality measures. The diagrams display rank-ordered distributions of betweenness centrality, closeness centrality, in-degree, and out-degree for the network associated with the eye-blinking task, as shown in Figure 8.

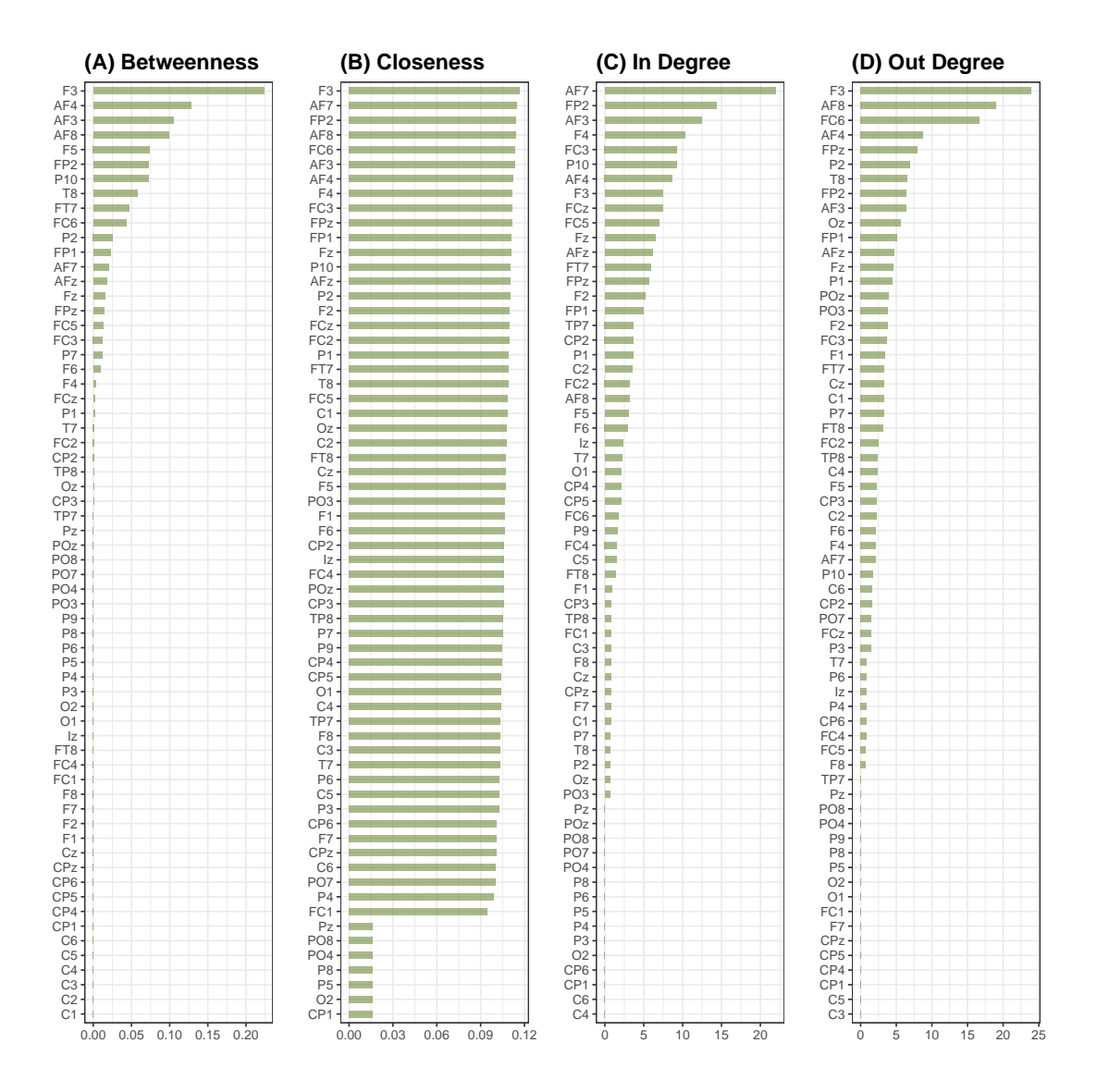


Figure 12: A comparison of centrality measures. Diagrams show rank-ordered distributions of betweenness, closeness, in degree and out degree for the network of horizontal eyeball movement task shown in Figure 8

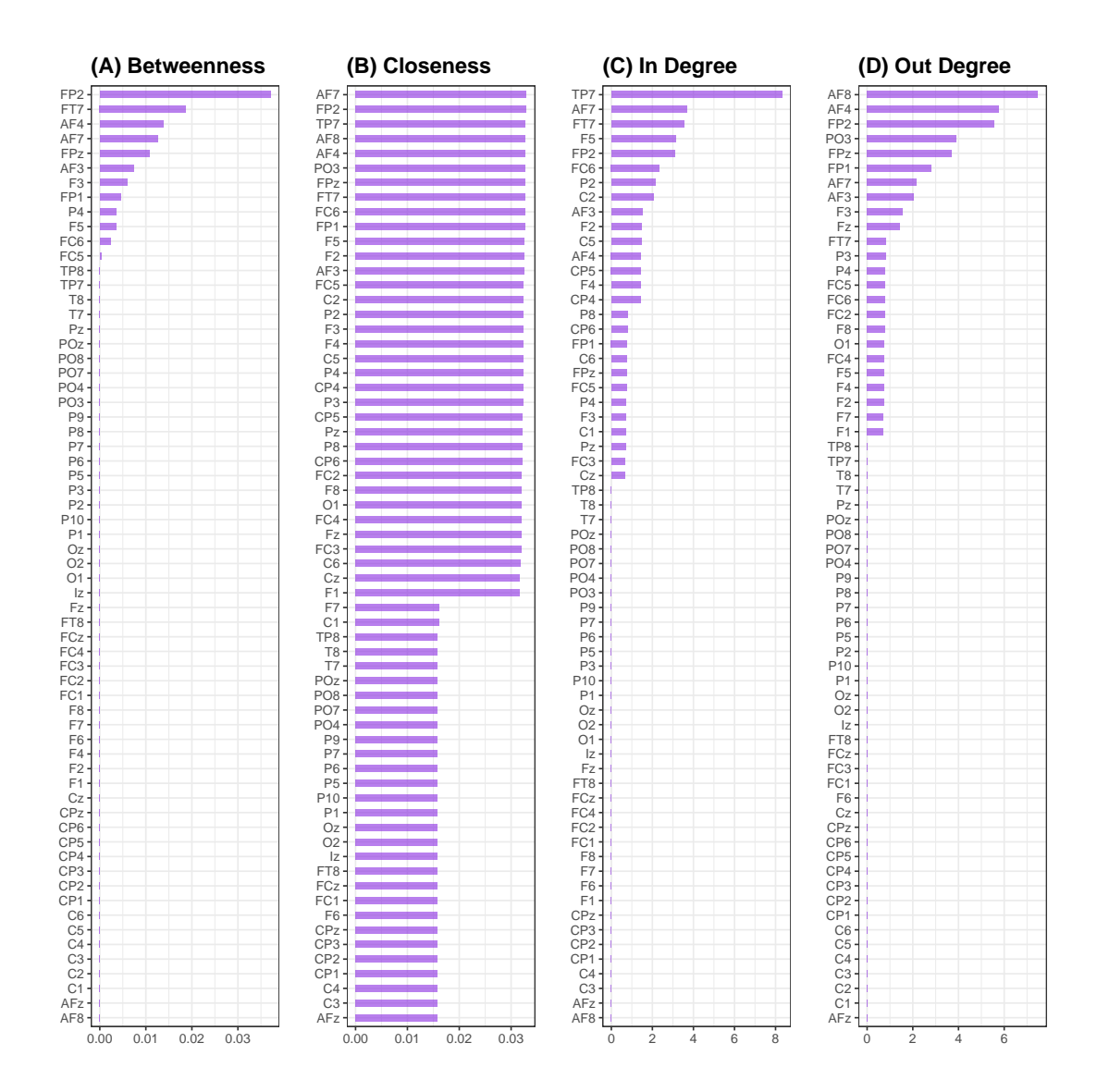


Figure 13: A comparison of centrality measures. Diagrams show rank-ordered distributions of betweenness, closeness, in degree and out degree for the network of vertical eyeball movement task shown in Figure 8